Charles University in Prague
Faculty of Mathematics and Physics
&
King's College London
Randall Division of Cell & Molecular Biophysics

DIPLOMA THESIS

Ondřej Mandula

Patterned Excitation Microscopy

Institute of Physics
Supervisor: Dr. Rainer Heintzmann
Consultant: Prof. RNDr. Jaromír Plášek, CSc.
Field of Study: Physics, Biophysics

2008

Title: Patterned Excitation Microscopy
Author: Ondřej Mandula
Department: Institute of Physics MFF UK
Supervisor: Dr. Rainer Heintzmann (Biological Nanoimaging research group, Randall Division, King's College London)
Supervisor's e-mail address: rainer.heintzmann@kcl.ac.uk
Abstract: The resolution of a fluorescent microscope is limited by diffraction to about 250 nm in the focal plane. Patterned Excitation Microscopy is a wide-field fluorescence microscopy method capable of surpassing the diffraction limit by a factor of two. A spatially modulated excitation of a sample is used to encode high Fourier frequency information into the acquired image. Post-acquisition processing extracts this information and leads to the enlargement of the detectable spatial frequencies area in Fourier space. This results in a resolution improvement in the reconstructed image. An algorithm for the image reconstruction and an experimental setup for data acquisition was developed. We achieved a 1.78 fold enlargement of the maximum detectable Fourier frequency in the experimental samples. This led to a FWHM of the reconstructed fluorescent bead profile more than 1.76 times smaller than in a wide-field image. Reconstructed images of real biological samples demonstrate the ability of this method to achieve a sectioning in the fluorescence microscope‘s wide-field mode.
Keywords: fluorescent microscopy, patterned excitation, resolution, Fourier transform

Název práce: Mikroskopie využívající prostorově modulovaného osvětlení
Autor: Ondřej Mandula
Katedra (ústav): Fyzikální ústav MFF UK
Vedoucí diplomové práce: Dr. Rainre Heintzmann (Biological Nanoimaging research group, Randall Division, King's College London)
e-mail vedoucího: rainer.heintzmann@kcl.ac.uk
Abstrakt: Difrakce limituje rozlišovací schopnost fluorescenčního mikroskopu na hodnotu zhruba 250 nm. Metoda presentovaná v této práci umožňuje rozlišení dvojnásobně zlepšit. Prostorově modulovaná excitace vzorku umožňuje rekonstruovat vysoké frekvence Fourierovy transformace pozorovaného objektu, které leží mimo detekční oblast klasické mikroskopie. Rozšíření oblasti detekovatelných frekvení Fourierovy transformace vede ke zlepšení rozlišení ve výsledném obrazu. Sestavili jsme aparaturu na snímání mikroskopických vzorků s prostorově modulovanou excitací a vyvinuli jsme program na rekonstrukci naměřených dat. Podařilo se nám detekovat 1.78 krát vyšší Fourierovské frekvence, což vedlo k 1.76 krát užšímu profilu (FWHM) rekonstruovaných fluorescenčních kuliček. Metodu jsme rovněž použili k rekonstrukci biologických preparátů.
Klíčová slova: fluorescenční mikroskopie, prostorově modulované excitace, rozlišovací schopnost, Fourierova transformace

Prohlašuji, že jsem svou diplomovou práci napsal samostatně a výhradně s použitím citovaných pramenů. Souhlasím se zapůjčováním práce.

I hereby declare that the thesis has been written by myself without any external unauthorised help. Any parts, words or ideas of the thesis, however limited, which are quoted from or based on other sources, have been acknowledged as such without exception. I grant Charles University in Prague the right to lend the thesis to other persons or institutions for educational or research purposes.

V Praze, 24. dubna 2008
Prague, 24 April 2008 Ondřej Mandula

Acknowledgment

First, I would like to thank my supervisor Rainer Heintzmann whose kind permission to participate on the project and his help to organize my stay in London was of paramount importance. His deep and penetrating views on Fourier theory, image processing and microscopy and his creative and original thinking was always a great source of inspiration.

I wish to thank Jaromír Plášek and PhD students Liisa Hirvonen and Kai Wicker for a valuable discussion and Jakub Nedbal for his overall support during my visits in London. A special thanks go to Elizabeth Ehler and Jiří Hašek for their beautiful samples presented in the thesis.

Thanks to Grant Agency of Charles University (grant no. 127407) and King's College London for the studentship on this project.

I appreciate a courage of Natalia Baker and others to read and suggest the improvements to this manuscript.

Finally, my deep gratitude goes to my parents. A short acknowledgment seems to be very little to thank for their support throughout my studies and life.

Contents

Preface

This work discusses a method for resolution improvement of the optical wide-field epifluorescence microscope. Resolution improvement is achieved by an enlargement of the area of detectable high spatial frequencies components in the Fourier transform.

This thesis is divided into six sections:

1. The introduction section gives a short overview of optical microscopy, a concept of the resolution, the Fourier theory of image formation and up-to-date high-resolution fluorescence microscopy techniques.

2. The second section introduces a theoretical concept of the method. Simulated data are used for the demonstration of individual steps of the image reconstruction.

3. The third section gives a description of the experimental setup used for the data acquisition of real samples.

4. The algorithm for the image reconstruction of acquired data is described stepwise in the fourth section.

5. In the fifth section the results from the simulated data as well as from real experimental samples are presented. A discussion of the results, possibilities and limits of the method is also included in this section.

6. The final section gives an overall summary of the project.

The thesis is supplemented with an appendix giving relevant mathematical definitions and theorems. There is also a description of some procedures used in the reconstruction algorithm. There are several reconstructed images in the last part of the appendix.

I participated on the presented project during a 9-month stay (October 2005 - June 2006) and successive shorter stays in October 2007 and February 2008 in the laboratory of the Biological Nanoimaging research group of the Randall Division, King's College London. I worked on the development of the reconstruction algorithm and the construction of the experimental setup. Experimental data presented in this thesis were acquired during my stay in London in February 2008.

1 Introduction

1.1 Optical microscopy

The naked human eye can differentiate one point object from another if the points are separated by a visual angle bigger than approximately 1.2 arc minute (equal to a distance ca. 0.35 mm at 1 m). Exploration of the world on a scale below this limit relies on the usage of instruments such as spectacles, magnifying glasses or microscopes. The forerunner of the compound microscope was invented in late 16^{th} century by Zacharias Janssen. Since then microscopy has undergone a long evolution. One of the milestones in the development of optical microscopy was the introduction of the Fourier theory into optics in the 19^{th} century. The pioneering works of Ernst Abbe [1] set a theoretical limit on the resolution of the microscope and helped to master the design of optical glass. Even though almost 400 years of sustained development is a long period of time, the number of scientific publications in recent years show, that this process is still ongoing.

1.2 Image of a Point Source

A description of the image formation in a microscope requires us to take the wave nature of light into account. In particular, we have to encounter diffraction effects. This section makes a short introduction into the problematics. This work focuses on fluorescence microscopy. Therefore, only incoherent imaging is discussed. A comprehensive description of the image formation using the Fourier theory can be found in [2].

An important characteristic of a microscope is an image of a point source. Let's assume we have a self-luminous, monochromatic point-like object (small volume of excited fluorophores emitting on the wavelength λ_{em}). An objective lens of the microscope can collect only a part of a spherical wave[1] emerging from the object. The objective transforms the wavefront into a truncated plane wave. The plane wave is refocused again into an image plane and creates a blurry spot rather than a point object. The distribution of the electric field $\vec{E}(\vec{r})$ in the image plane, which is created by interference of the focused beam, is called an Amplitude Point Spread Function (APSF). An intensity of the image is proportional to the square of the amplitude of the electric field $I(\vec{r}) \propto \left|\vec{E}\right|^2$. The profile of the intensity distribution in the image plane is called the Point Spread Function (PSF). For an objective with a circular pupil, it is referred to as the Airy pattern. In scalar theory it is given by [2]:

$$PSF(\rho) = I_0 \left(2\frac{J_1(\alpha\rho)}{\alpha\rho}\right)^2, \tag{1.1}$$

[1] For reasons of simplicity we ignore the detailed distribution of the field close to the fluorophores (field of the oscillating dipole) and assume the wave to be perfectly spherical.

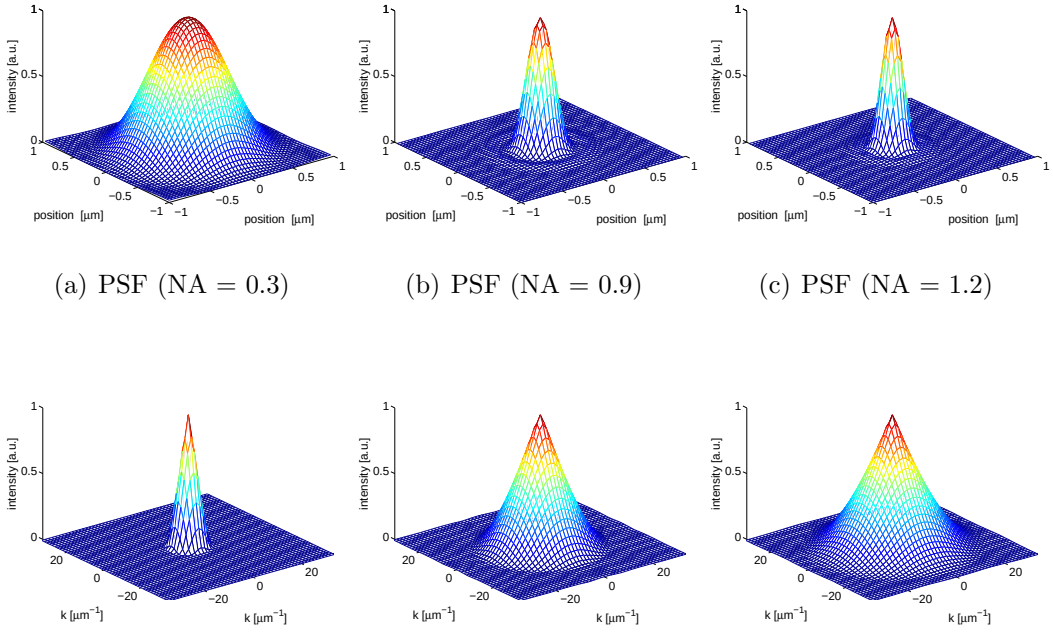

(a) PSF (NA = 0.3) (b) PSF (NA = 0.9) (c) PSF (NA = 1.2)

(d) OTF (NA = 0.3) (e) OTF (NA = 0.9) (f) OTF (NA = 1.2)

Figure 1.1: *PSF (a - c) and corresponding OTF (d - e) for objectives with different NA. The emission wavelength* $\lambda_{em} = 510$ nm. *Note the reciprocal relation between the size of the PSF and the corresponding OTF. Spatial confinement of one leads to the delocalization of the other.*

where I_0 is the normalizing constant, J_1 is the Bessel function of the first kind of order one, ρ is the distance from the center of the image and α depends on the parameters of the setup and the wavelength of the emitted light λ_{em}:

$$\alpha = \frac{2\pi}{\lambda_{em}} \mathrm{NA}$$

NA is the numerical aperture of the objective:

$$\mathrm{NA} = n \sin \vartheta \tag{1.2}$$

where n is the refractive index of the immersion medium and ϑ is the half-angle of the maximum cone of light that can enter the objective lens.

Eq.(1.1) holds for a low-NA scalar approximation. A high NA vectorial description of the PSF can be found in [3]. Simulated PSFs for an in-focus plane and aberration-free objectives with various NA are shown in Fig. 1.1 (a-c). Both the shape and size of the PSF determines the image of the observed sample as under assumption of linearity of the system, any object might be decomposed into a set

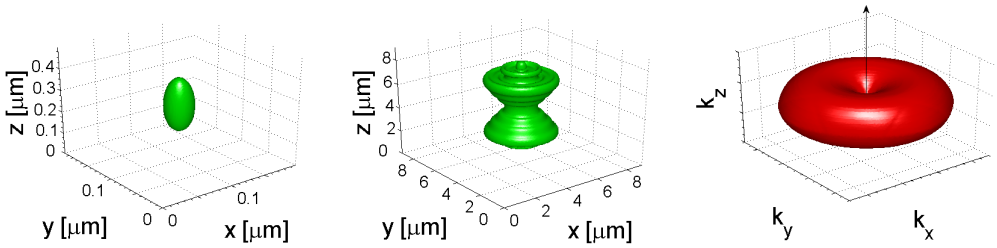

(a) (b) (c)

Figure 1.2: *Simulated 3D wide-field PSF and OTF for* $\lambda_{em} = 510$ nm *and a water immersion objective* NA $= 1.2$. *An iso-intensity surface of the PSF on the (a) 90% and (b) 1% of the maximum intensity. (c) A support of the OTF. Note the 'missing cone' along the axial direction (black arrow).*

of arbitrary small areas (points). Each of this points can be imaged independently creating the PSF in a particular position and with a particular intensity. The final image is readily obtained by a sum of these individual images. (This operation is mathematically described by a convolution. It is discussed in section 2.2.) Full 3D simulation of the PSF is given in Fig. 1.2.

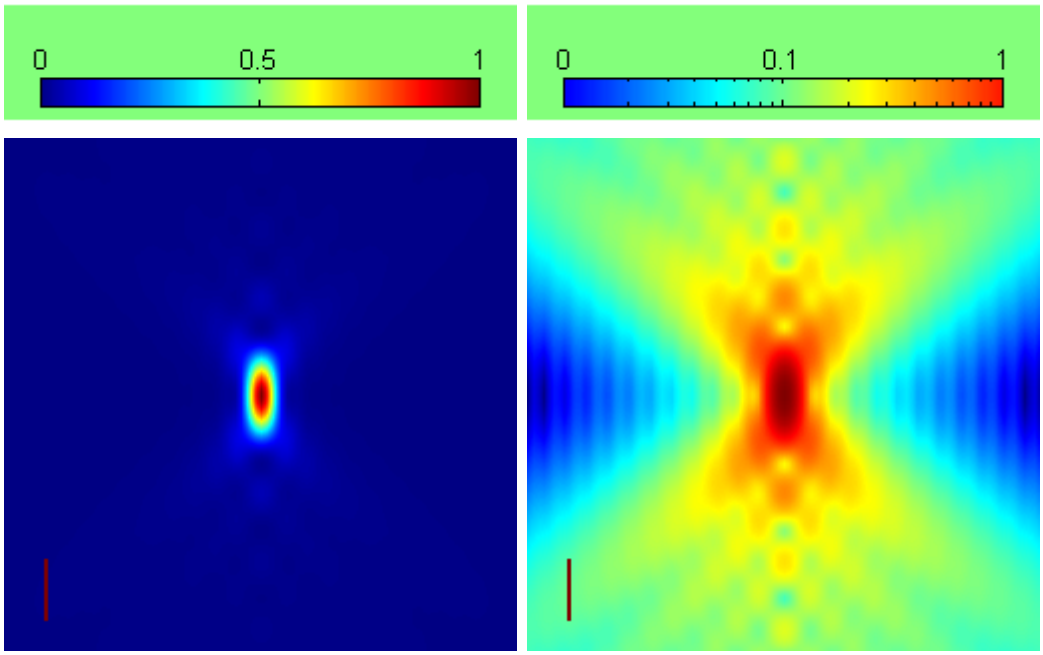

(a) Linear scale (b) Log scale

Figure 1.3: *Axial slice of the PSF for objective NA = 1.2 and* $\lambda_{em} = 510$ nm. *Intensity [a.u.] shown in pseudo - color (a) linear and (b) logarithmic scale. Axial axis along vertical direction. Scale bar* 500 nm.

The Fourier transform (see Appendix A, Eq.(A.4)) of the PSF is called the Optical

Transfer Function (OTF):

$$\mathcal{F}\left\{PSF(\vec{r})\right\}(\vec{k}) \equiv OTF(\vec{k}). \tag{1.3}$$

There are three OTFs computed for objectives with different NA shown in Fig. 1.1(d-

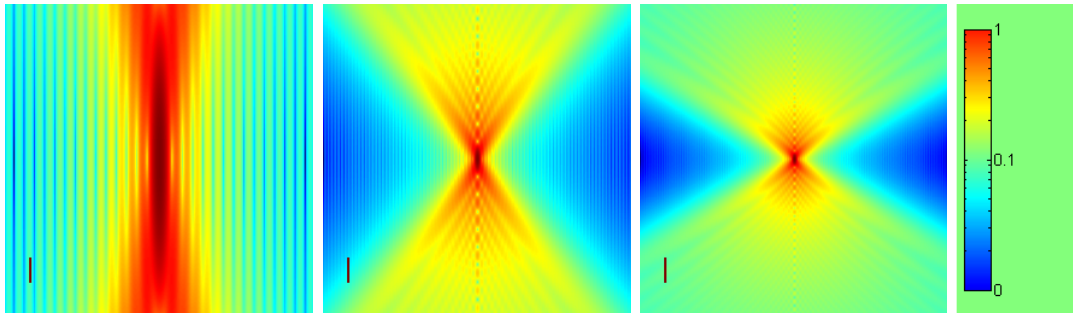

(a) PSF (NA = 0.3) (b) PSF (NA = 0.9) (c) PSF (NA = 1.2)

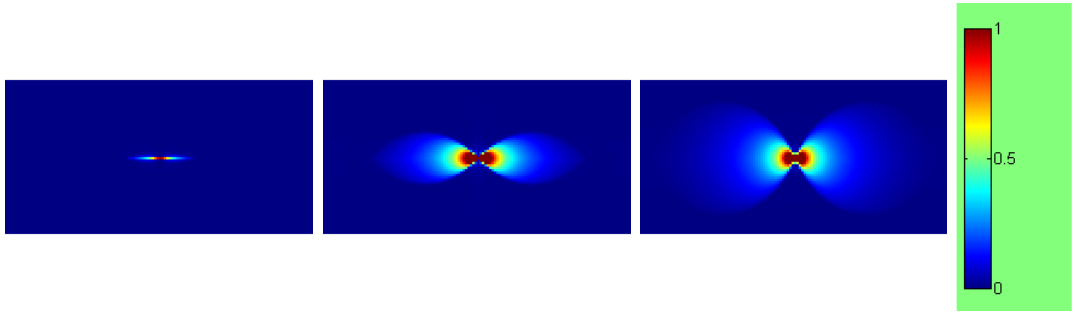

(d) OTF (NA = 0.3) (e) OTF (NA = 0.9) (f) OTF (NA = 1.2)

Figure 1.4: *Axial slices of the PSF for water immersion objectives with numerical apertures (a) NA = 0.3, (b) NA = 0.9 and (c) NA = 1.2.* $\lambda_{em} = 510$ nm. *Intensity [a.u.] shown in logarithmic scale on the right. Scale bar* 3 μm. *Corresponding OTF displayed in (d-f). Images show the magnitude [a.u.] of the OTF in linear scale on the right. The z-axis is along the vertical direction.*

f). We observe that a localization of the PSF in real space (narrow peak) leads to a delocalization of the OTF (broad peak) in Fourier space and vice versa. In general, the OTF is always zero for high spatial frequencies of the Fourier transformation. In other words the microscopy system acts as a low pass filter for spatial frequencies in the Fourier transform. A full three-dimensional OTF is non-zero within a doughnut-like region (support) as shown in Fig. 1.2(c). An absence of Fourier components along the axial direction (k_z axis) is the so called 'missing cone' problem (see also Fig. 5.13 on page 53). A comparison of the OTFs computed for objectives with different NA is shown in Fig. 1.4(d-f).

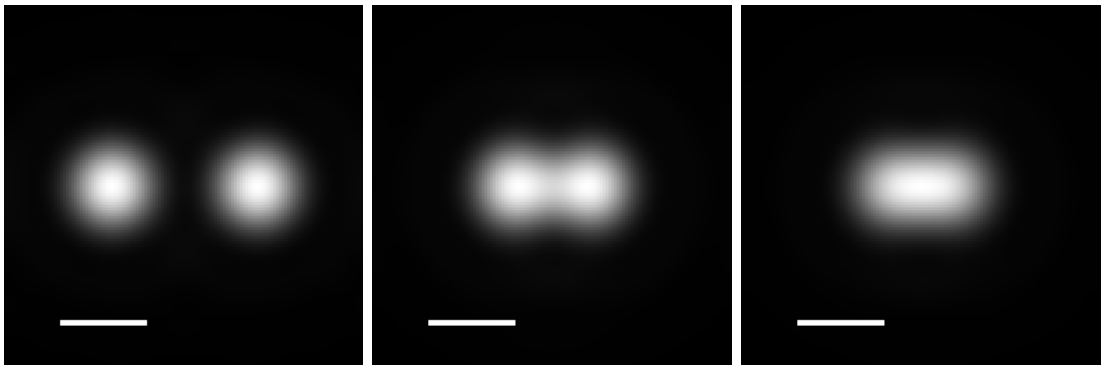

(a) Two separated points (b) Raleigh limit (c) Sparrow limit

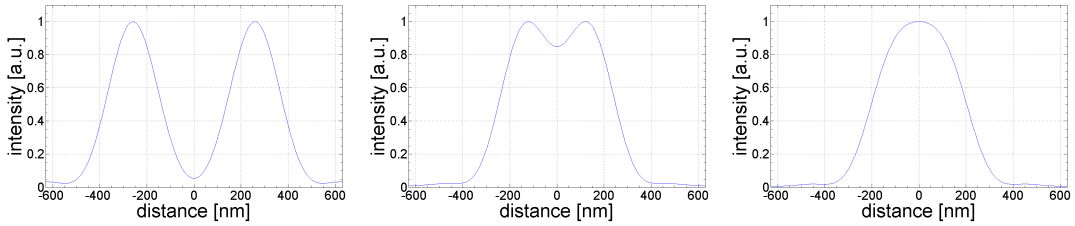

(d) Two separated points (e) Raleigh limit (f) Sparrow limit

Figure 1.5: *Two point sources separated by the distance* $2d_{Raleigh}$ *(a),* $d_{Raleigh}$ *(b), and* $d_{Sparrow}$ *(c) with corresponding intensity profiles (d-f). Simulated for a water immersion objective NA = 1.2 and* $\lambda_{em} = 510$ nm. *Scale bar 200 nm.*

1.3 Resolution in Microscopy

An image of two point-like self-luminous (mutually incoherent) objects in a focus plane will be a sum of two corresponding PSFs. As they get close to each other, their images blend and eventually join together into one elongated blurry spot (Fig. 1.5). The resolution of a microscope is defined as the minimum distance of separation between the two point objects in order to 'resolve' them as two individual entities in the image. As the ability to resolve two objects in the image depends on the observer, there is the so called Rayleigh resolution limit which defines the resolution in the lateral plane as the distance between the maximum of the Airy function (see Eq.(1.1)) and its first minimum. This means that two points can just be resolved if one point sits in the position of the first minimum of the Airy function of the second point (Fig. 1.5(b)). For an aberration free system, the Rayleigh limit is determined by the numerical aperture (NA) of the objective lens and by the wavelength of the emitted light λ_{em}:

$$d_{Rayleigh} \approx 0.61 \frac{\lambda_{em}}{\mathrm{NA}}. \tag{1.4}$$

Separation of two points by $d_{Rayleigh}$ still results in a dip of the intensity profile (about 27% below the peak value) on the intersection between two maxima in the image (Fig. 1.5(e)). These points can actually still be resolved as two individual

entities (see Fig. 1.5(b)). Another definition of resolution is the distance where the dip in the intensity profile vanishes. This is the Sparrow resolution limit:

$$d_{Sparrow} \approx 0.47 \frac{\lambda_{em}}{\mathrm{NA}} \tag{1.5}$$

and is demonstrated in Fig. 1.5 (c and f).

There are technical limits on manufacturing of objectives and the highest numerical aperture used in fluorescence microscopy imaging is around NA = 1.4 for oil-immersion lenses. From Eq.(1.4) (or Eq.(1.5)) we see that even for high NA objectives (NA>1.0) the minimum required distance in the lateral plane between two point-like objects is at best roughly half the wavelength of the light emitted by fluorophores (10^2−10^3nm). In the axial direction the required minimum distance is about three times bigger (see Fig. 1.4). The distance in the range of visible light wavelength (10^2−10^3nm) corresponds to the scale of the interior organelles of a cell and hence it is difficult or impossible to image fine details of sub-cellular features with a classical fluorescence microscope.

1.4 Resolution and High Frequencies of the Fourier Transformation

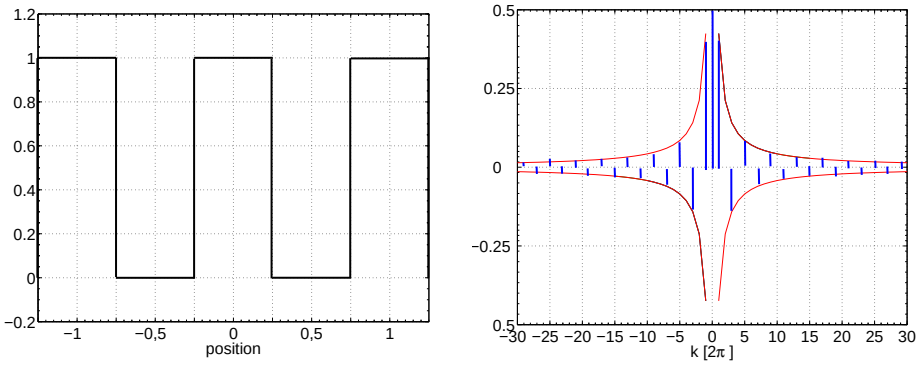

(a) Square Grid (b) Fourier transform of the grid

Figure 1.6: *Infinitely long square grid (a) and its Fourier transform (b). The Fourier transform is represented by blue spikes. Red solid line represents the envelope of the spikes.*

As mentioned in section 1.2, a microscopy system acts as a low-pass filter for spatial frequencies in the Fourier transform. This section gives a demonstration of how the resolution in a microscopic image is linked to the high frequencies of the Fourier transform of a sample structure.

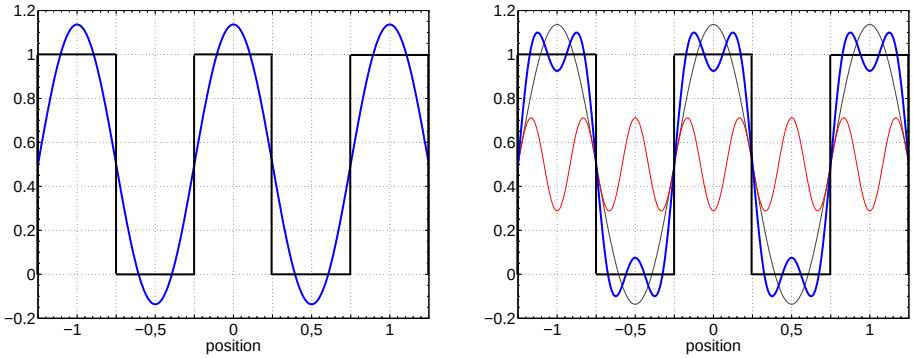

(a) N=1 (b) N=2

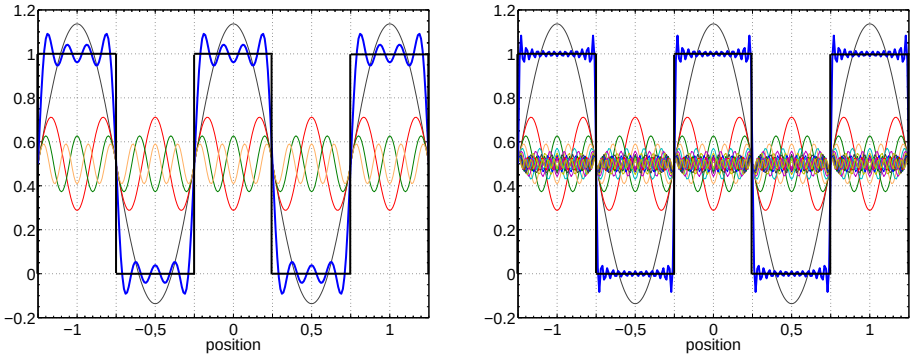

(c) N=4 (d) N=14

Figure 1.7: *Sum of the Fourier components (thick blue solid line) for increasing number N in the sum Eq.*(1.6). *Each cosine function is plotted with the general offset a_0.*

An infinitely long periodic square-grid $g(x)$ with a period $p = 1$

$$g(x) = \begin{cases} 1 & x \in \left\langle -\frac{p}{4} + mp,\ \frac{p}{4} + mp \right\rangle;\ m \in \mathbb{Z} \\ 0 & \text{else} \end{cases}$$

represents an idealized structure (Fig. 1.6(a)). This function can be approximated (see Appendix A, Eq.(A.1)) by the sum of the harmonic functions (components):

$$g(x) \approx \sum_{n=-N}^{N} a_n e^{ik_n x}. \tag{1.6}$$

where $k_n = 2\pi n$ and coefficients a_n we obtain from the Fourier transform of $g(x)$

over a period p. For the grid $g(x)$ we get (see Appendix A, Eq.(A.2)):

$$\begin{aligned} a_0 =& 0.5 \\ a_n =& \begin{cases} \frac{1}{|n|\pi} & |n| \text{ odd} \\ 0 & |n| \text{ even} \end{cases} \end{aligned} \tag{1.7}$$

The Fourier transform of the grid $g(x)$ (Fig. 1.7(b)) is a set of individual spikes symmetrical (complex conjugated) with respect to a vertical axis. Each spike (in general complex) represents a component in the Eq.(1.6) and carries information about the frequency k_n (position on the k-axis), the amplitude a_n (length of the spike) and the phase (complex value).

In this example all coefficients a_n are real and $a_n = a_{-n}$. A pair of components for n and $-n$ then represents a cosine function

$$a_{-n}e^{-k_n x} + a_{+n}e^{+k_n x} = 2a_n \cos(k_n x);\ a_{-n} = a_{+n} \equiv a_n \tag{1.8}$$

with amplitude $2a_n$ and spatial frequency $k_n = 2\pi n$. We can then rewrite Eq.(1.6) as a sum of cosine functions:

$$g(x) = a_0 + \sum_{n=1}^{N} 2a_n \cos(2\pi n x) \tag{1.9}$$

In Fig. 1.7 we can observe how the sum Eq.(1.9) with increasing N converges towards the original function $g(x)$. A zero component ($n = 0$, a spike in a position $k = 0$ in Fig. 1.6(b)) represents a general offset of the function. It is a constant $a_0 = 0.5$, $k_0 = 0$. First two spikes close to the zero (in position $k = \pm 2\pi$ in Fig. 1.6(b)) represent a cosine function with spatial frequency $k_1 = 2\pi$ and amplitude $2a_1 = \frac{2}{\pi}$. This low-frequency cosine function caries basic information about the periodicity of the function, but the approximation of the sharp edges of the grid is very crude (Fig. 1.7(a)). Increasing number N in the sum Eq.(1.9) leads to adding cosine functions with increasing spatial frequencies $k_n = n2\pi$ (Fig. 1.7(b-d)). We can see that the edges of the original function become approximated nicely (except for the area very close to the edge where the Fourier series exceeds the original function. This is so called Gibbs phenomenon [4]). If we want to get a good approximation of the sharp transitions (edges) or small details in the original function we have to add in the sum Eq.(1.9) harmonic functions with high spatial frequencies k_n.

There is further demonstration of this phenomenon in Fig. 1.8. If we remove in the sum Eq.(1.9) the low frequency cosine function ($n = 1$, $k_1 = 2\pi$) and sum the remaining components we observe that the approximation of the original function severely deteriorates but information about the sharp edges is still present (see Fig. 1.8(a)). We can determine the edges even after the removal of several low-frequency components (Fig. 1.8(b)). This demonstrates that the high-frequency components of the Fourier transform carry information about the details in the sample.

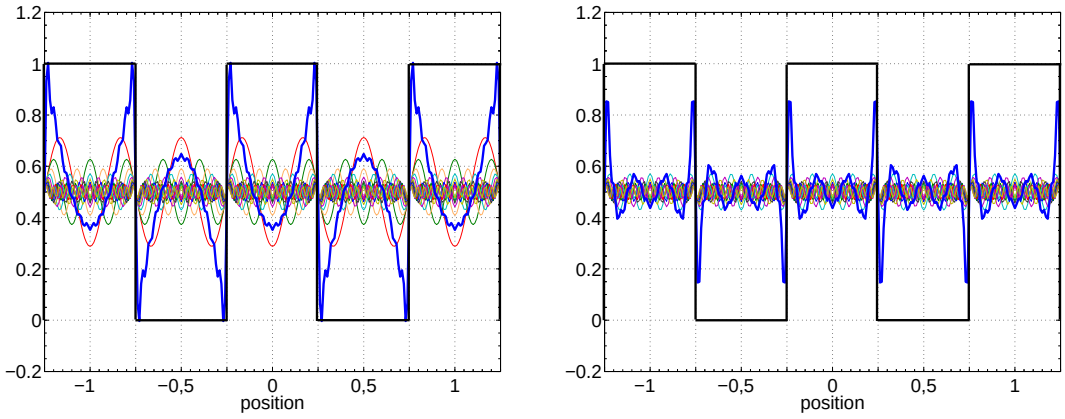

(a) (b)

Figure 1.8: *Removal of low-frequency cosines components in Eq.*(1.9) *leads to deterioration of the approximation of the original function but the information about the edges is still contained. (a) Cosine function with* $k_1 = 2\pi$ *removed from the sum. (b)First four low-frequency cosines (*$n = 1,\ 2,\ 3$ *and* 4*) removed. The sum of the remaining components is plotted as a thick blue solid line.*

A two-dimensional demonstration of the same phenomenon with a non-periodic function is shown in Fig. 1.9. We can observe a loss of detail in the image if the high frequency Fourier components are removed (Fig. 1.9(a-c) and corresponding Fig. 1.9(e-g)). The removal of the low frequency components in Fig. 1.9(d) causes the brightness and contrast of the image to deteriorate but the details in the structure are still visible in Fig. 1.9(h).

The ability to resolve small structure under a microscopic observation is thus closely related to the ability of a microscope to pass through high frequency components of the Fourier transform of the observed structure.

1.5 Fluorescence Microscopy

Fluorescence microscopy is an invaluable tool in modern cell biology. It is a non-invasive method of imaging the interior of living specimen with multicolor molecular labels (fluorophores) of high specificity. As light in the visible spectral range is usually used for an excitation of the fluorophore, fluorescence microscopy is less harmful for biological samples than high-resolution techniques such as electron microscopy. Unfortunately, spatial resolution of a fluorescence microscope is subject to a fundamental limit caused by a diffraction [1] which limits the size of an observable object in fluorescence microscopy.

In the last 15 years several methods have been proposed to bypass the diffraction

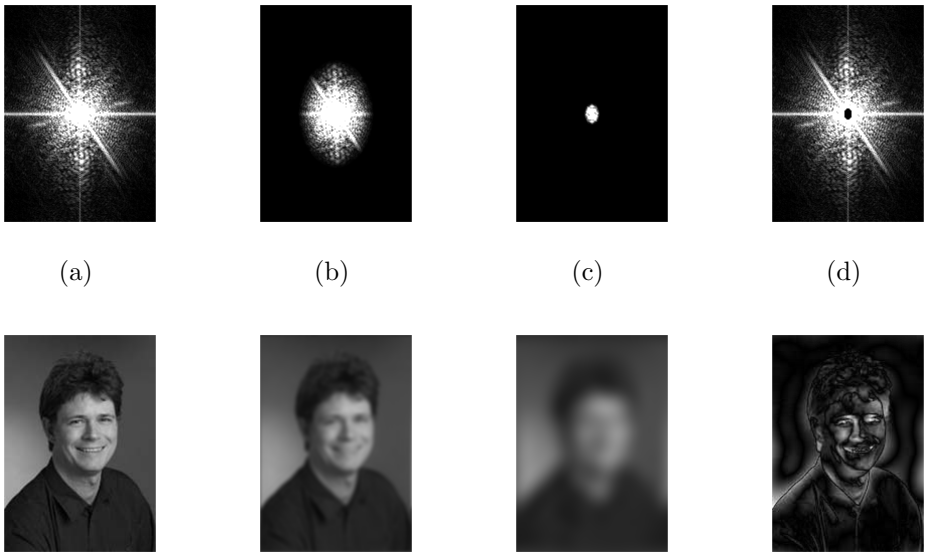

(a) (b) (c) (d)

(e) (f) (g) (h)

Figure 1.9: *Image (a) is a full area (100%) of the Fourier Transform, in (b) maximum spatial frequencies are reduced by 50%, in (c) by 90% and in the image (d) low frequencies (5%) are removed. Corresponding Inverse Fourier Transforms in (e-g). (Courtesy of Rainer Heintzmann)*

limit in fluorescence microscopy imaging. From a technical point of view they can be divided into two branches: scanning microscopy and wide-field (non-scanning) microscopy.

1.5.1 Scanning fluorescence microscopy

In scanning fluorescence microscopy a beam of illumination light is focused into a small spot and swept over a sample. The sample is divided into discrete array (pixels) and a fluorescent signal from each pixel is collected as the focused beam passes through it. The whole discrete (3D) array of recorded intensities creates a microscopic image of the sample. The focused spot - a three-dimensional PSF (Fig. 1.2(a,b)) - has a complex 3D shape elongated along the axial direction. Enhancing the resolution in scanning microscopy then requires squeezing down the volume of excited fluorophores in the scanning process (STED [5], 4Pi type A or in combination with interference effect in the detection part 4Pi type C [6]) or rejecting photons coming from areas distant from a geometrical focal point of the scanning spot (confocal microscopy [7]).

Confocal microscopy is a popular method in biological research. The idea was patented in 1957 by M. Minsky but it was not applicable until the 1970s when suitable light sources became available. In 1968 the use of a spinning disk with an array

of pinholes for an illumination as well as for a 'confocal' detection was proposed [8]. In 1971 a laser-illumination scanning confocal microscope was introduced [9]. A confocal microscope is one which has a pinhole inserted in a point optically conjugated (confocal) with a geometrical point of focus of an objective. A confocal point is a position of a point source image. In the approximation of geometrical optics it is the point where rays of a diverging beam coming from the point source (fluorophore) are brought into focus. This means that fluorescent photons generated by the scanning spot in a close proximity to the geometrical focal point can pass through the pinhole placed in the confocal point. Photons coming from distant areas (laterally and axially) from the geometrical focal point are effectively blocked by the pinhole as their conjugated points are in different positions. This provides a true 3D sectioning in thick samples as all the out-of focus haze is removed. Resolution improvement in a lateral direction is minor and only occurs if operated with a pinhole that is significantly smaller than the Airy disk [10]. Such a small pinhole discards not only the undesired out-of-focus light but also much of the light coming from the focal plane. In weakly fluorescent biological samples this can be a strongly limiting factor.

4Pi microscopy employs two opposing objective lenses exciting a sample and collecting fluorescence from both sides of the sample plane. Adding the second opposing objective increases the numerical aperture of the system and two counter propagating coherent beams focused into the same position interfere with each other which sharpens the focused spot. This central spot is accompanied by two axially shifted side-lobes (coming from interference). It leads to a replication artefacts in the raw data. The side-lobes can be partially suppressed using a confocal detection by one of the objective (4Pi type A) or the incoherent fluorescent light is collected by both of the objectives and is allowed to interfere on the detector (4Pi type C). Using a two-photon excitation can further decrease the relative strength of the side-lobes. The rest of the side-lobes is removed computationally with a deconvolution technique. A sevenfold improvement of the axial resolution ($\backsim$ 80 nm) over confocal microscopy has been reported in [11].

STED (Stimulated Emission Depletion) microscopy is based on a stimulated emission depletion process using two synchronized ultra-fast pulse lasers. One pulse is focused in a sample and excites fluorophores in a diffraction limited volume. The second pulse in a doughnut shape with a 'hole' in the center (also diffraction limited) is delivered with a time delay within the fluorescence lifetime of the fluorophore. It causes the depletion of the excited state through stimulated emission. The saturated depletion confines fluorescence only to the center of the doughnut, where the depletion pulse has zero intensity (hole). A lateral resolution down to 28 nm has been reported in [12].

1.5.2 Wide-field fluorescence microscopy

Contrary to the scanning methods, wide-field microscopy is a technique where the whole field of view of an objective is recorded in one camera shot or viewed by the

eye of an observer. No scanning in the lateral plane is needed which speeds up data acquisition and no fluorescence photons are discarded in the detection process which makes wide-field methods more light efficient. This is an advantage especially in microscopy imaging of sensitive and weakly fluorescent biological samples. There are several techniques for resolution improvement of a wide-field microscope.

A wide-field counterpart of 4Pi microscopy is I^nM fluorescence microscopy [13]. A fluorescent sample is mounted between two opposing objectives which are focused into the same focal plane within the sample. Each objective collect a fluorescent signal from one side of the focal plane and creates a magnified image. These images are superimposed on a single CCD camera. The optical pathway of the fluorescence signal is adjusted to be equal for both objectives. This results in an interference of the two beams from every single fluorophore with each other. The recorded interference pattern contains high resolution information about the axial position of the fluorescent molecule. This method is called 'image interference microscopy' (I^2M). If the sample is illuminated through both objectives, a high-resolution axial illumination pattern is created because of the interference of the two illuminating beams. As incoherent light is used for the illumination the method is named 'incoherent interference illumination microscopy' (I^3M). Combination of I^2M and I^3M at the same time is referred to as 'incoherent interference illumination - image interference microscopy' (I^5M). Axial resolution better than 100 nm has been reported [13].

The method described in this work is another wide-field microscopy method which enhances the resolution in both axial and lateral directions. The resolution improvement is achieved by restoring high spatial frequencies in the Fourier transform of the observed structure that would normally lie out of the pass-band of a classical wide-field microscope. The use of a spatially modulated illumination of the sample to obtain sectioning was proposed in 1997 [21] and in following years a number of papers were published proposing the use of the method for resolution improvement along a lateral as well as axial direction. In literature the method is referred to by several names such as 'structured illumination microscopy' (SIM) [23, 14] (combination of SIM and I^5M is referred to as I^5S [15]), 'harmonic excitation light microscopy' (HELM) [16], 'laterally modulated excitation microscopy' (LMEM) [17] and 'patterned excitation microscopy' (PEM) [24]. This final name is the one used throughout this thesis.

2 Patterned Excitation Microscopy - theoretical background

2.1 Fluorophore emission

In a two-state system (omitting a triplet state), the flux of photons Ψ_{em} emitted from the first excited singlet state of a fluorophore is given by [19, 20]:

$$\Psi_{em} = C\frac{\Psi_{ex}}{\frac{1}{\sigma\tau} + \Psi_{ex}}, \tag{2.1}$$

where σ and τ are the absorption cross section and the fluorescence lifetime of the fluorophore, respectively. Ψ_{ex} is a flux of excitation photons and C is a constant independent on the photon flux. If the excitation photon flux is low: $\Psi_{ex} \ll \frac{1}{\sigma\tau}$, Eq.(2.1) gives a linear relationship between the excitation and emission:

$$\Psi_{em} = C\sigma\tau\Psi_{ex}. \tag{2.2}$$

The intensity of light is directly proportional to the photon flux $I \propto \Psi$ and so we can rewrite Eq.(2.2) in terms of intensities:

$$I_{em} = QI_{ex}, \tag{2.3}$$

where I_{em} and I_{ex} are the excitation and emission intensities, respectively. Q is a constant independent on the intensity.

In the presence of a triplet state, the saturation behavior is slightly changed [24], but it does not alter the essential characteristics of the fluorescence emission and the relation Eq.(2.3) holds.

The linear relation Eq.(2.3) (low intensities of excitation light) is assumed in the theory described below. A non-linear case (allowing higher resolution improvement) is discussed in [24, 25].

This work discusses a resolution improvement along (one or several) lateral directions. An extension to 3D has special aspects some of which are discussed in section 5.

2.2 Linear system model

The aim of fluorescence microscopy imaging is to record the spatial distribution of fluorophores in a sample.

We can define a local concentration of the fluorophores as

$$\rho(\vec{r}) = \frac{\Delta N_F(\vec{r})}{\Delta V}, \tag{2.4}$$

where ΔN_F is the number of fluorophores in a small volume ΔV. The mesoscopic volume ΔV is small compared to the sample and the resolution limit of the microscope, but large enough compared to the molecular scale of the fluorophore. In the linear case of Eq.(2.3), we get a local fluorescence intensity:

$$I_{em}(\vec{r}) = Q\Delta N_F(\vec{r})I_{ex}(\vec{r}),$$

and using Eq.(2.4):

$$I_{em}(\vec{r}) = Q\Delta V\rho(\vec{r})I_{ex}(\vec{r}). \tag{2.5}$$

We can assume the volume ΔV to be a constant corresponding to the sampling. Since we are only interested in a relative intensity we can leave out all multiplicative constants in Eq.(2.5) and write:

$$I_{em}(\vec{r}) = \rho(\vec{r}) \cdot I_{ex}(\vec{r}). \tag{2.6}$$

Light emitted by fluorescent molecules is mutually incoherent. Then we can express an image $Im(\vec{r})$ recorded by a microscope (diffraction limited, linear optical system) as a spatial convolution of the fluorescent intensity emitted by the sample structure $I_{em}(\vec{r})$ with the intensity point spread function $PSF(\vec{r})$ of the optical system:

$$Im(\vec{r}) = I_{em}(\vec{r}) \circledast PSF(\vec{r}). \tag{2.7}$$

The convolution operation is denoted by the symbol "$\circledast$". Eq.(2.7) assumes a spatially invariant PSF.

Combining Eq.(2.6) and Eq.(2.7) yields:

$$Im(\vec{r}) = [\rho(\vec{r}) \cdot I_{ex}(\vec{r})] \circledast PSF(\vec{r}). \tag{2.8}$$

In Fourier space (using convolution theorem (Appendix A.4) and Eq.(1.3)):

$$\mathcal{F}\{Im(\vec{r})\}(\vec{k}) \equiv \tilde{Im}(\vec{k}) = \left[\tilde{\rho}(\vec{k}) \circledast \tilde{I}_{ex}(\vec{k})\right] \cdot OTF(\vec{k}). \tag{2.9}$$

2.3 Optical Transfer Function

A wide-field $OTF(\vec{k})$ has a finite convex support ($supp\,(OTF) \equiv \left\{\vec{k};\ OTF(\vec{k}) \neq 0\right\}$). In Fourier space it means that in any direction $\vec{\sigma} = \frac{\vec{k}}{|\vec{k}|}$ from the origin ($\vec{k} = 0$) there is a certain border (cut-off) frequency $k_{cut}(\vec{\sigma})$ beyond which $OTF(\vec{k}) = 0$; $\left(\left|\vec{k}\right| > \mathrm{k_{cut}}(\vec{\sigma})\right)$. An illustration for a situation in a focal plane is in Fig. 1.1(d-f). A 3D situation is shown in Fig. 1.2(c) and Fig. 1.4(d-f). For an aberration free optical system with a circular aperture in a focal plane $k_{cut}(\vec{\sigma})$ is a constant determined by the numerical aperture of the objective NA and the wavelength of emitted light λ_{em}:

$$k_{cut} = 2\frac{2\pi}{\lambda_{em}}\mathrm{NA}. \tag{2.10}$$

In 2D $supp\,(OTF)$ is a circle with k_{cut} as a radius. In a 3D situation, the OTF support creates an interesting doughnut-like object (Fig. 1.2(c)).

Because of the multiplication of the Fourier transform of the structure with the OTF in Eq.(2.9), an optical system acts as a low-pass filter for spatial frequencies in Fourier space. All frequencies beyond k_{cut} are effectively lost after the multiplication.

2.4 Classical microscopy

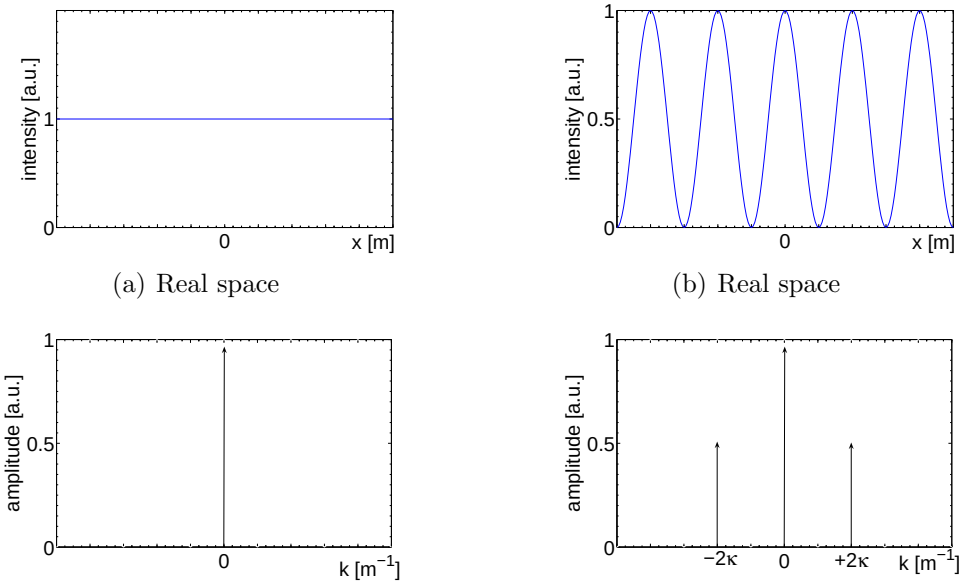

(a) Real space (b) Real space

(c) Fourier space (d) Fourier space

Figure 2.1: *(a) Constant and (b) spatially modulated illumination intensity profile with Fourier transforms (c) and (d), respectively.*

In a classical wide-field fluorescence microscope an even illumination (excitation) over the whole area of a sample is used:

$$I_{ex}\left(\vec{r}\right) = const. \equiv I_0.$$

Then in Fourier space

$$\tilde{I}_{ex}(\vec{k}) = I_0\delta(\vec{k}) \tag{2.11}$$

where $\delta(\vec{k})$ is a Dirac's delta distribution. This is demonstrated in Fig. 2.1(a and c).

Substituting Eq.(2.11) into Eq.(2.9):

$$\tilde{Im}(\vec{k}) = \left[\tilde{\rho}(\vec{k}) \circledast I_0\delta(\vec{k})\right] \cdot OTF(\vec{k})$$

and after performing the convolution:

$$\tilde{Im}(\vec{k}) = I_0 \cdot \tilde{\rho}(\vec{k}) \cdot OTF(\vec{k}). \tag{2.12}$$

As a wide-field $OTF(\vec{k})$ has a finite support (see section 2.3), the multiplication $\tilde{\rho}\cdot OTF \equiv \tilde{\rho}_0$ in Eq.(2.12) leads to the loss (cut-off) of any spatial frequency information of the $\tilde{\rho}(\vec{k})$ that is beyond the k_{cut}. A one-dimensional illustration is in Fig. 2.2.

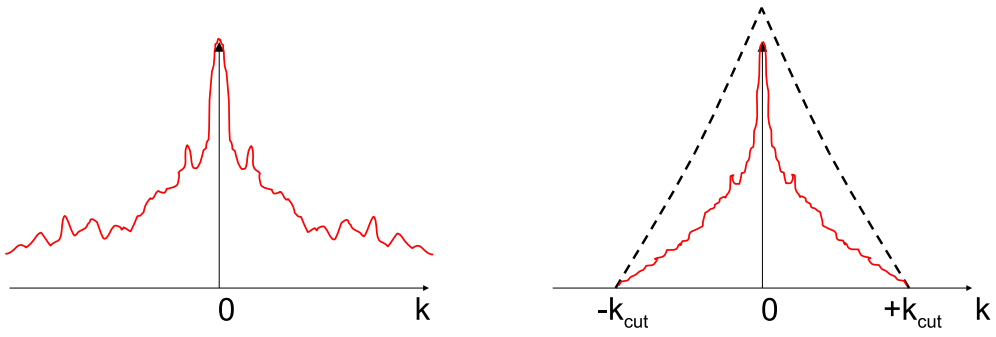

(a) Classical Component (b) Multiplication with OTF

Figure 2.2: *(a) Classical component in Fourier space. (b) After multiplication with the OTF (black dashed line) all Fourier frequencies beyond k_{cut} are lost.*

2.5 Patterned Excitation Microscopy

2.5.1 Excitation of the sample with spatially modulated intensity

In Patterned Excitation Microscopy (PEM) a spatially modulated (pattern) intensity $I_{ex}(\vec{r})$ is used for an excitation of a fluorescent sample. This section will demonstrate a principle of the method on an example where a harmonic excitation pattern with a sinusoidal profile is imposed upon the sample. Modification of the pattern is discussed in section 2.6.

We assume the intensity of excitation light in the in-focus plane to vary as:

$$I_{ex}\left(\vec{r}\right) = \frac{I_0}{2}\left(1 + \cos(2\vec{\kappa}\cdot\vec{r} + \phi_0)\right) \tag{2.13}$$

where $\frac{I_0}{2}$, $2\vec{\kappa}$ and ϕ_0 are the amplitude, the spatial frequency and the initial phase of the excitation pattern, respectively. The intensity profile of Eq.(2.13) is shown in Fig. 2.1(b). The Fourier transformation of the Eq.(2.13) results in a sum of three delta peaks. One is located in the origin and two are symmetrically shifted sideways to the position of $\pm 2\vec{\kappa}$ in Fourier space (Fig. 2.1 (d). Two-dimensional demonstration is shown in Fig. 2.4).

$$\tilde{I}_{ex}(\vec{k}) = \frac{I_0}{2}\left[\delta(\vec{k}) + \frac{1}{2}\left(e^{i\phi_0}\delta(\vec{k}+2\vec{\kappa}) + e^{-i\phi_0}\delta(\vec{k}-2\vec{\kappa})\right)\right]. \tag{2.14}$$

Convolution of $\tilde{\rho}$ and $\tilde{I_{ex}}$ (see Eq.(2.9)) leads to a sum of three identical copies of the classical component mutually shifted in Fourier space into positions of the δ peaks

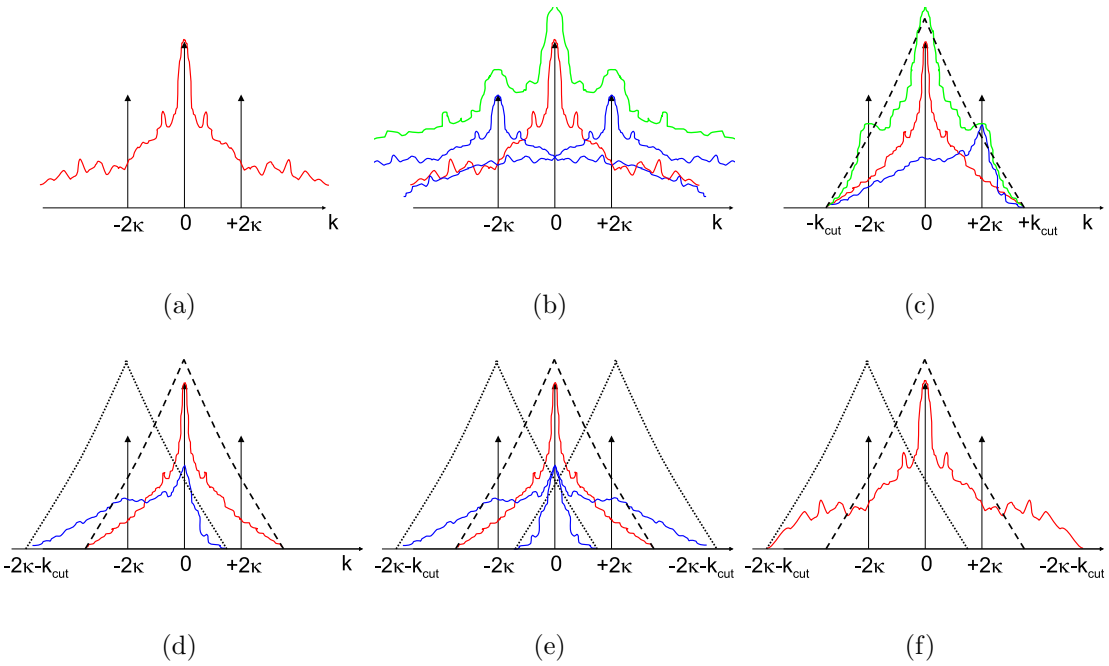

Figure 2.3: *Illustration of the PEM theory. (a) A classical component (red line). (b) A classical component (red) with two side components (blue) located in* $\pm 2\kappa$*. We detect a sum of all components (green). (c) The highest detectable Fourier frequency after multiplication with the OTF (black dashed line) is* k_{cut} *(for the sake of simplicity, one side component was omitted). The side components (blue) are cut asymmetrically with respect to their 'true zero frequency'. (d) Shift of the side component (blue) to the the correct position of the 'true zero frequency'. (e) Shift of both components. (Shifted OTFs in black dotted line.) (f) Recombination of all components (red) with an weighted averaging. The maximal detectable Fourier frequency is shifted to* $k_{cut} + 2\kappa$ *(compare with Fig. 2.2(b)). An enlarged area of detectable frequencies leads to the resolution improvement of the reconstructed image (the inverse Fourier transform of recombined components (red)).*

(see Eq.(A.12) in Appendix A):

$$\tilde{Im}(\vec{k}) = \frac{I_0}{2}\left[\tilde{\rho}(\vec{k}) + \frac{1}{2}\left(e^{i\phi_0}\tilde{\rho}(\vec{k}+2\vec{\kappa}) + e^{-i\phi_0}\tilde{\rho}(\vec{k}-2\vec{\kappa})\right)\right] \cdot OTF(\vec{k}). \qquad (2.15)$$

Note that each copy has a different complex amplitude determined by the initial phase ϕ_0. The situation is illustrated in Fig. 2.3(b, c).

The first term (a zero order component) in Eq.(2.15), corresponds to the classical wide-field component shown in Fig. 2.3(a). The multiplication with the *OTF* leads again to the cut-off of the high frequencies above k_{cut} and thus the frequency content is the same as in the classical case (Eq.(2.11)).

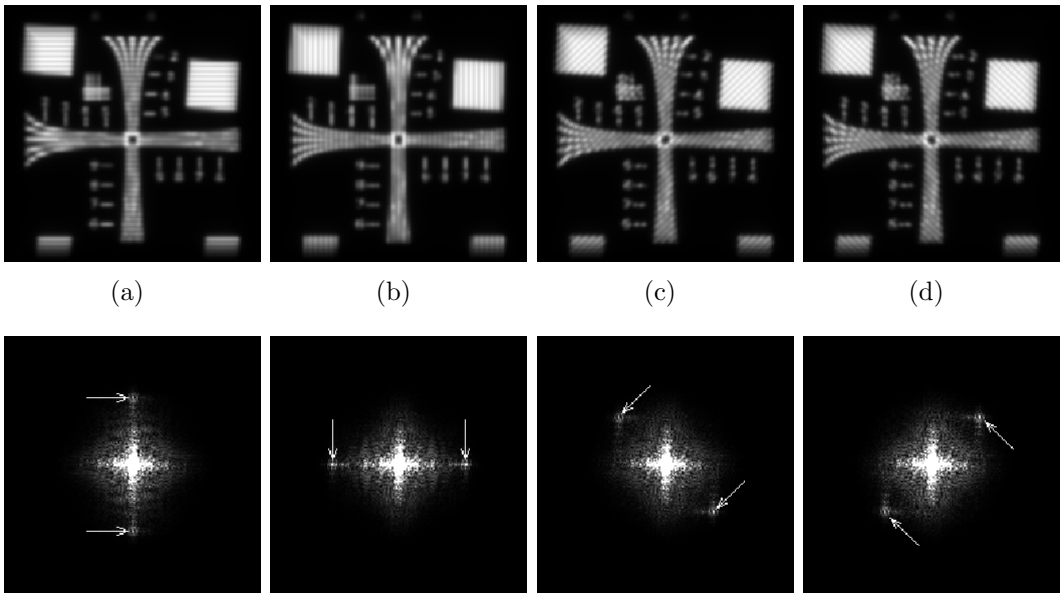

(a) (b) (c) (d)

(e) (f) (g) (h)

Figure 2.4: *Simulated data. Four orientations of the illumination pattern projected on the sample (a) 0˚, (b) 90˚ (c) 135˚ and (d) 225˚. (e-h) Corresponding Fourier transforms. Peaks in the Fourier transform pointed with white arrows.*

We define a classical component $\tilde{\rho}_0(\vec{k})$ as follows

$$OTF(\vec{k}) \cdot \tilde{\rho}(\vec{k}) \equiv \tilde{\rho}_0(\vec{k}). \tag{2.16}$$

A convolution of $\tilde{\rho}(\vec{k})$ with the side-shifted delta peaks $e^{\pm i\phi_0}\delta(\vec{k} \pm 2\vec{\kappa})$ results in the displacement of $\tilde{\rho}(\vec{k})$ in Fourier space to the position $\vec{k} = \pm 2\vec{\kappa}$ (second and third term in the Eq.(2.15)). This situation is illustrated in Fig. 2.3 (b). Moreover, these side-shifted components are multiplied with a complex constant $e^{\mp i\phi}$ and finally multiplied with the OTF (Fig. 2.3(b)). We define ± 1 components by:

$$\begin{aligned} e^{i\phi_0}\tilde{\rho}(\vec{k} + 2\vec{\kappa}) \cdot OTF(\vec{k}) \equiv & e^{i\phi_0}\tilde{\rho}_{-1}(\vec{k}), \\ e^{-i\phi_0}\tilde{\rho}(\vec{k} - 2\vec{\kappa}) \cdot OTF(\vec{k}) \equiv & e^{-i\phi_0}\tilde{\rho}_{+1}(\vec{k}). \end{aligned} \tag{2.17}$$

Due to the symmetry property of the Fourier transform for real images (see Eq.A.6) we get

$$\tilde{\rho}_0(\vec{k}) = \overline{\tilde{\rho}}_0(-\vec{k}) \,\text{and}\, \tilde{\rho}_{+1}(\vec{k}) = \overline{\tilde{\rho}}_{-1}(-\vec{k}).$$

Before a multiplication with the OTF these side-shifted components are exact copies of the classical component $\tilde{\rho}_0$ (ignoring a multiplicative constant) as shown in Fig. 2.3 (b). The multiplication with the OTF in the Eq.(2.15) or Eq.(2.17) leads to an asymmetrical cut-off of these side components with respect to their 'true zero frequency' (located in $\pm 2\vec{\kappa}$). On one side the cut-off is closer to the 'true

zero frequency' than in the case of the classical component $\tilde{\rho}_0$. However, on the opposite side the cut-off is actually pushed further which allows it to pass through the frequencies which lie beyond the cut-off limit in the classical wide-field case. The asymmetrical cut-off is shown in Fig. 2.3 (c).

If we separate the individual components $\tilde{\rho}_{\pm 1}$ in Eq.(2.15) we can align them in Fourier space with the classical component $\tilde{\rho}_0$, so that their 'true zero frequency' is placed back in the origin as demonstrated in Fig. 2.3(d-e). This requires translation of the $\tilde{\rho}_{\pm 1}$ by $\pm 2\vec{\kappa}$ and compensation for the complex amplitude $e^{\pm i\phi_0}$ (see Eq.(2.17)). Then we gain information about the Fourier frequencies beyond the original k_{cut} (in the direction of vector $\pm 2\vec{\kappa}$). The cut-off frequency border in the direction of the vector $\pm 2\vec{\kappa}$ then increases to

$$k_{cut}^{final} = k_{cut} + |2\vec{\kappa}| \tag{2.18}$$

as illustrated in Fig. 2.3 (f).

2.5.2 Component separation

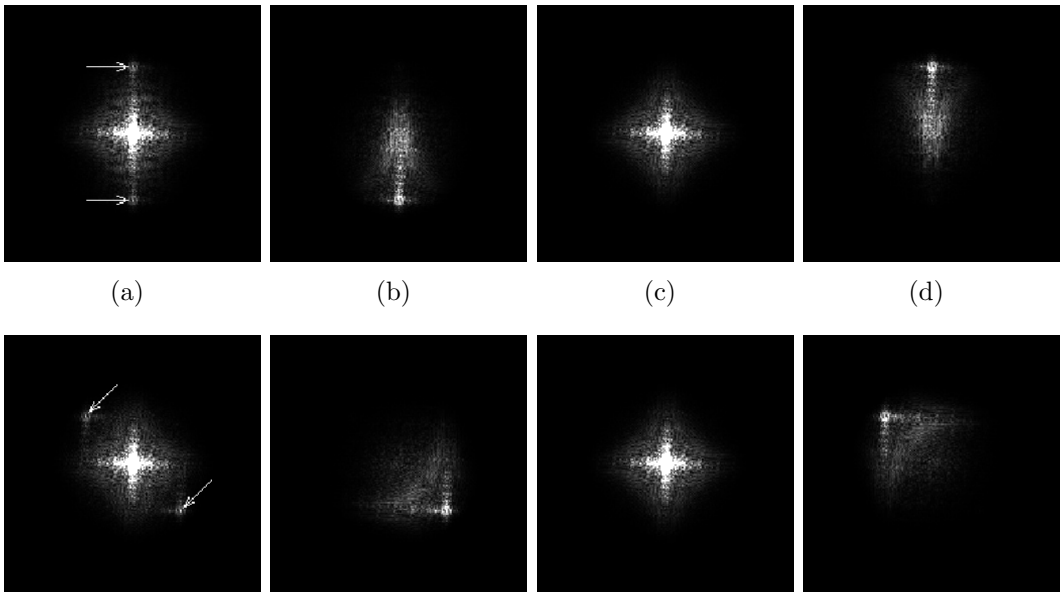

Figure 2.5: *Simulated data. Separation of the individual components for two orientations of the illumination pattern (0° and 135°). (a, e) The Fourier transform of the data with arrows pointing to the δ peaks. (b, f) component $\tilde{\rho}_{-1}$, (c, g) component $\tilde{\rho}_0$ (d, h) component $\tilde{\rho}_{+1}$ from Eq.*(2.20).

In general, to separate M components we need to take $N \geq M$ images Im^n, $(n = 1..N)$ for different positions of the excitation pattern I_{ex}^n, $(n = 1..N)$ with respect to the sample. In case of the sinusoidal pattern Eq.(2.13), we have to acquire at least

$N \geq 3$ images to be able to separate $M = 3$ components ($\tilde{\rho}_0$ and $\tilde{\rho}_{\pm 1}$). We can, for example, shift the pattern by equal steps $n\frac{p}{N}$, $(n = 1..N)$, where $p = \frac{2\pi}{2|\vec{\kappa}|}$ is a spatial period of the pattern. Then the excitation pattern can be expressed as follows

$$I_{ex}^{n}(\vec{r}) = \frac{I_0}{2}\left[1 + \cos\left(2\vec{\kappa}\cdot(\vec{r} + n\frac{p}{N}) + \phi_0\right)\right];\ (n = 1..N) \tag{2.19}$$

or in Fourier space:

$$\tilde{I}_{ex}^{n}(\vec{k}) = \frac{I_0}{2}\left[\delta(\vec{k}) + \frac{1}{2}\left(e^{-i\left(2\frac{2\pi}{N}n+\phi_0\right)}\delta(\vec{k}+2\vec{\kappa}) + e^{\left(2\frac{2\pi}{N}n+\phi_0\right)}\delta(\vec{k}-2\vec{\kappa})\right)\right];\ (n = 1..N).$$

After the convolution in Eq.(2.9) we get modified Eq.(2.15):

$$\tilde{Im}^{n}(\vec{k}) = \left[B_0\tilde{\rho}_0(\vec{k}) + B_{-1}e^{-i\left(2\frac{2\pi}{N}n+\phi_0\right)}\tilde{\rho}_{-1}(\vec{k}) + B_{+1}e^{i\left(2\frac{2\pi}{N}n+\phi_0\right)}\tilde{\rho}_{+1}(\vec{k})\right];\ (n = 1..N) \tag{2.20}$$

where B_m is a magnitude of the m-th component. This is a set of N linear equations for M unknown components $\tilde{\rho}_m$, $(M \leq N)$. In a vector notation:

$$\vec{\tilde{Im}} = \mathbb{A}\cdot\vec{\tilde{\rho}}, \tag{2.21}$$

where

$$\begin{aligned}\vec{\tilde{\rho}} =&(B_{-1}e^{i\phi_0}\tilde{\rho}_{-1},\ B_0\tilde{\rho}_0,\ B_{+1}e^{-i\phi_0}\tilde{\rho}_{+1}),\\ \vec{\tilde{Im}} =&(\tilde{Im}^1,\ \tilde{Im}^2,\ \tilde{Im}^3),\end{aligned} \tag{2.22}$$

and $\mathbb{A}$ is $N \times M$ separation matrix:

$$A_{nm} = \exp\left\{i2\frac{2\pi}{N}(n-1)\left[(m-1) - \frac{M-1}{2}\right]\right\};\ (n = 1..N,\ m = 1..M). \tag{2.23}$$

Separated components can be found by the inversion of Eq.(2.21):

$$\vec{\tilde{\rho}} = \mathbb{A}^{-1}\cdot\vec{\tilde{Im}}. \tag{2.24}$$

If the matrix A_{nm} is not squared ($M < N$), a pseudo-inverse matrix approach is used. There are three separated orders for two orientations of the excitation pattern shown in Fig. 2.5.

2.5.3 Component alignment

Components $\vec{\tilde{\rho}}$ (Eq.(2.22)) separated in Eq.(2.24) need to be shifted to the appropriate position in Fourier space to align them with $\tilde{\rho}_0$ (Fig. 2.3(e)) and be corrected for the initial phase of the pattern ϕ_0 (Eq.(2.17)). We define

$$\begin{aligned}\tilde{\rho}_{-1}^{shift}(\vec{k}) =&\tilde{\rho}_{-1}(\vec{k} - 2\vec{\kappa}),\\ \tilde{\rho}_{0}^{shift}(\vec{k}) =&\tilde{\rho}_{0}(\vec{k}),\\ \tilde{\rho}_{+1}^{shift}(\vec{k}) =&\tilde{\rho}_{+1}(\vec{k} + 2\vec{\kappa}).\end{aligned} \tag{2.25}$$

Values of $2\vec{\kappa}$ and ϕ_0 can (in principle) be determined from the parameters of the pattern Eq.(2.13). In real experiment they are determined from the comparison of the individual separated orders (see section 4.7).

2.5.4 Recombination of separated components

Separated (Eq.(2.24)) and shifted (Eq.(2.25)) components have to be recombined to yield the final Fourier transform of the reconstructed image. Within the area where the individual separated components $\tilde{\rho}_m(\vec{k})$ overlap they must be combined with appropriate weights $w_m(\vec{k})$. A Wiener filter approach is used in order to reduce noise artefacts:

$$W(\vec{k}) = \frac{\sum_{m=-1}^{+1} w_m(\vec{k}) \tilde{\rho}_m^{comp}(\vec{k})}{\gamma + \sum_{m=-1}^{+1} w_m(\vec{k})} \tag{2.26}$$

where γ is the Wiener parameter and $\tilde{\rho}_m^{comp}$ is the separated component compensated for the multiplication with the OTF in Eq.(2.16) and Eq.(2.17) and the magnitude B_m in Eq.(2.20).

If we define a shifted OTF to the position of the m-th delta peak

$$OTF_m(\vec{k}) = OTF(\vec{k} + m2\vec{\kappa}) \tag{2.27}$$

then

$$\tilde{\rho}_m^{comp}(\vec{k}) = \frac{1}{\left|OTF_m(\vec{k})\right| B_m} \tilde{\rho}_m^{shift}(\vec{k}) \tag{2.28}$$

If we want to alter the 'strength' of the particular components we can, for example, modify the magnitude B_m in Eq.(2.28).

2.5.5 Noise consideration in the weighted averaging

The weights $w_m(\vec{k})$ in Eq.(2.26) can be computed as the inverse variance

$$w_m = \frac{1}{\sigma_m^2(\vec{k})} \tag{2.29}$$

of the $\tilde{\rho}_m^{comp}(\vec{k})$. Poisson noise in real space makes noise independent on frequency in the Fourier transform $\sigma^2(\vec{k}) = const.$ [32]. This can bee seen from the following arguments. An intensity fluctuation in one pixel (in a position p) of the recorded image in real space can be seen as an amplitude (A) fluctuation of the delta peak $A\delta_p(x)$ sitting in the position p. The Fourier transform of the delta peak

$$\mathcal{F}\left\{A(x)\delta_p(x)\right\} = A(p)e^{ikp}$$

is a complex plane wave (with an amplitude A) expanded all over Fourier space. This means that a fluctuation in one pixel in real space results in a fluctuation over

all pixels in Fourier space. The amplitude of the fluctuation $A(p)$ in Fourier space will be independent on the position k.

If we have multiple pixels (p_i) in the image $Im(p_i)$ in real space, the fluctuations of $\tilde{Im}(k)$ in Fourier space will add up individually

$$\tilde{Im}(k) = \sum_{p_i} A(p_i) e^{ikp_i}$$

As the independently fluctuating quantities are the amplitudes $A(p_i)$ (not p_i) the variance of the fluctuation will be independent on k. Thus $\sigma^2(\vec{k}) = const.$

Then, for the compensated $\tilde{\rho}_m^{comp}$ (see Eq.(2.28))

$$\sigma_m = \frac{\sigma}{\left|OTF_m(\vec{k})\right| B_m} \tag{2.30}$$

and using the weights Eq.(2.29) we can rewrite Eq.(2.26) as follows

$$W(\vec{k}) = \frac{\sum_{m=-1}^{+1} \left|OTF_m(\vec{k})\right| B_m \tilde{\rho}_m^{shift}(\vec{k})}{\gamma + \sum_{m=-1}^{+1} \left(\left|OTF_m(\vec{k})\right| B_m\right)^2}. \tag{2.31}$$

2.5.6 Apodization

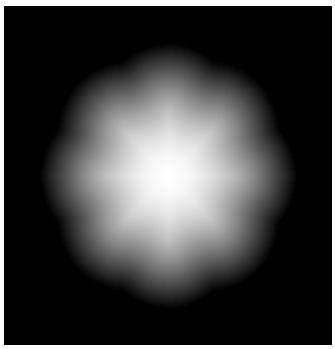

Figure 2.6: *Computed h_{goal} apodization function. Shown in linear scale.*

The reconstructed Fourier transformation is obtained from $W(\vec{k})$ in Eq.(2.31). A final apodization function $h_{goal}(\vec{k})$ is used to shape the reconstructed Fourier transform and to reduce artefacts that can occur in a reconstructed image.

$$\tilde{\rho}^{final}(\vec{k}) = W(\vec{k}) \cdot h_{goal}(\vec{k}). \tag{2.32}$$

According to [26] h_{goal} the function minimizing the second moment of the PSF projected along any direction (in plane) is

$$h_{goal}^{\cos}(\vec{k}) = \begin{cases} \cos\left(\frac{\pi}{2} \frac{|\vec{k}|}{k_{cut}^{final}}\right); & |\vec{k}| \leq k_{cut}^{final}(\vec{\sigma}) \\ 0; & |\vec{k}| > k_{cut}^{final}(\vec{\sigma}) \end{cases} \tag{2.33}$$

where $\vec{\sigma} = \frac{\vec{k}}{|\vec{k}|}$. This apodization function is shown in Fig. 2.6 with the intensity profile plotted in Fig. 2.7. Alternatively other apodization functions can be used:

$$h^q_{goal}(\vec{k}) = \begin{cases} \left(1 - \frac{|\vec{k}|}{k^{final}_{cut}}\right)^q; & |\vec{k}| \leq k^{final}_{cut}(\vec{\sigma}) \\ 0; & |\vec{k}| > k^{final}_{cut}(\vec{\sigma}) \end{cases} \tag{2.34}$$

By choosing different values of parameter q we can alter the reconstructed Fourier transform. A demonstration of different profiles of the apodization function is in Fig. 2.7.

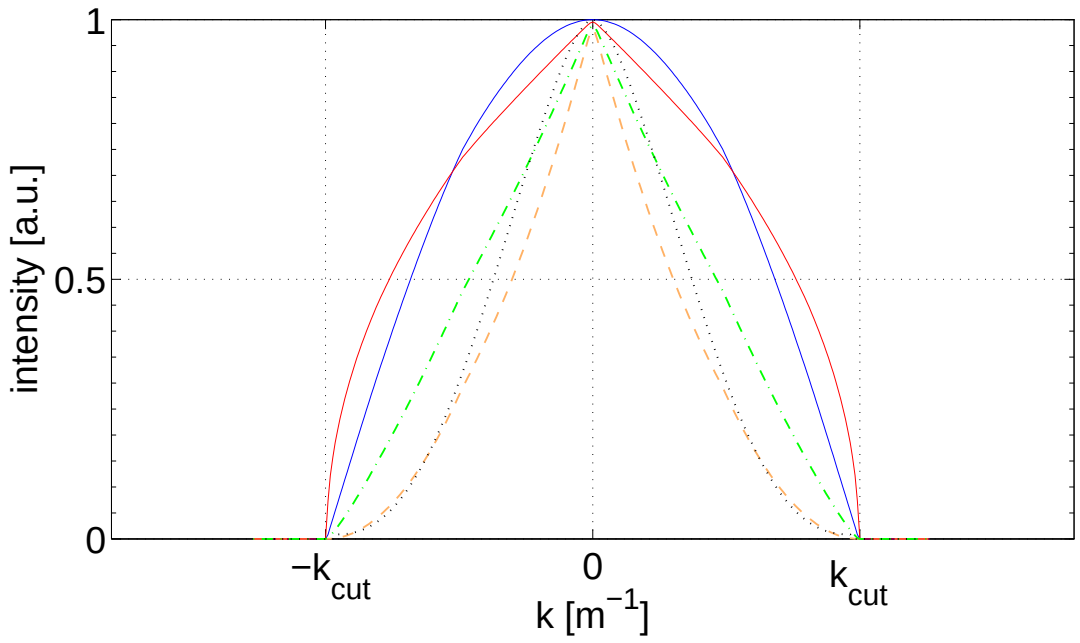

Figure 2.7: *Profiles of the apodization function h_{goal}. The sinusoidal profile of $h^{\cos}_{goal}$ (Eq.(2.33)) is plotted as a blue solid line. The apodization functions h^q_{goal} computed according to Eq.(2.34) for $q = 0.5$ (red solid line), $q = 1.2$ (green dot-and-dash line) and $q = 2$ (yellow dash line). The theoretical OTF computed for the reconstructed k_{cut} frequency is plotted with the black dotted line.*

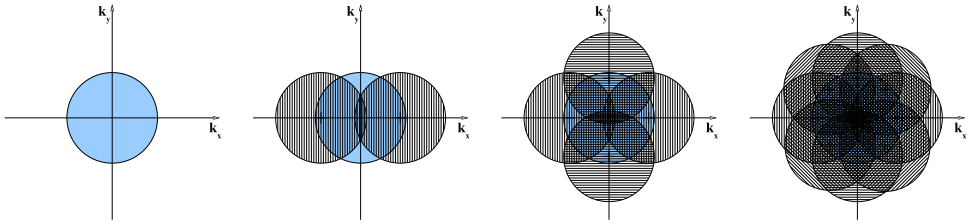

(a) (b) (c) (d)

Figure 2.8: *Enlargement of a support of the OTF. (a) The support of the classical wide-field OTF. (b) Enlargement of the support along the k_x axis results in a resolution improvement along the x direction. (b) Enlargement along the k_x and k_y axis. (c) Enlargement in four directions results in an isotropic resolution improvement.*

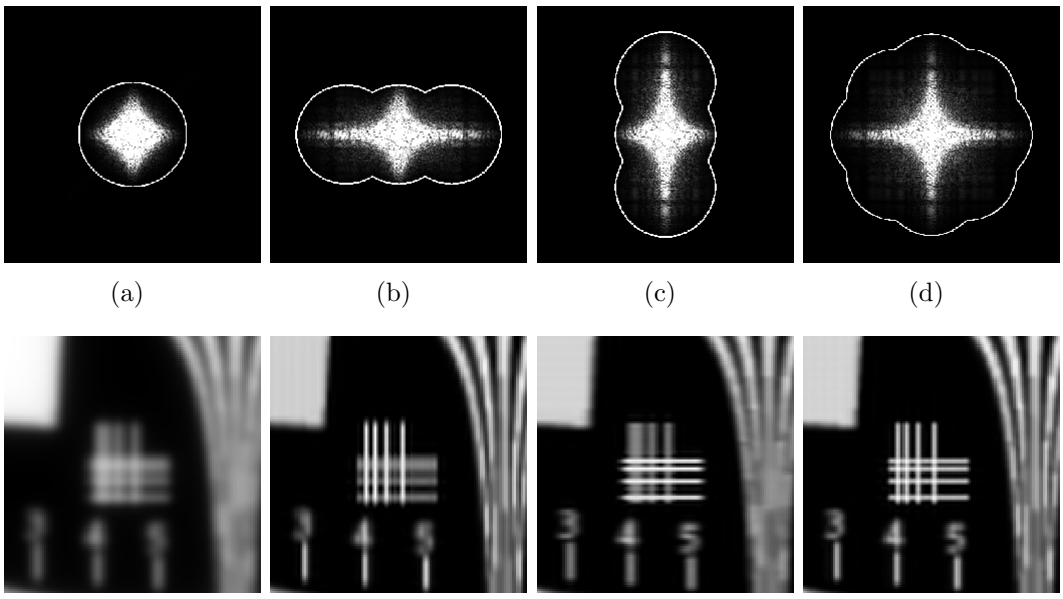

(a) (b) (c) (d)

(e) (f) (g) (h)

Figure 2.9: *Detail of the simulated data. (a) The Fourier transform of a wide-field image. (b) Reconstruction of the Fourier transform along one direction 0˚ (c) 90˚ (d) Combination of reconstructions along directions 0˚, 45˚, 90˚ and 135˚. Borders of the reconstructed OTF support visualized with a white line. (d - h) Inverse Fourier transforms of (a-d), respectively. (f) The resolution improvement along the direction 0˚ allows to resolve individual vertical lines, horizontal lines stay unresolved. (g) Vertical lines unresolved, horizontal resolved. (h) The isotropic resolution improvement.*

2.5.7 Final reconstruction

The reconstructed image in real space $\rho^{final}(\vec{r})$ is obtained by the inverse Fourier transform of $\tilde{\rho}^{final}(\vec{k})$ (Eq.(2.32))

$$\rho^{final}(\vec{r}) = \mathcal{F}^{-1}\left\{\tilde{\rho}^{final}(\vec{k})\right\}(\vec{r}). \tag{2.35}$$

Since we have extended the region of detectable spatial frequencies in Fourier space (Eq.(2.18) and Fig. 2.8), the resolution in the reconstructed image is enhanced (see section 1.4).

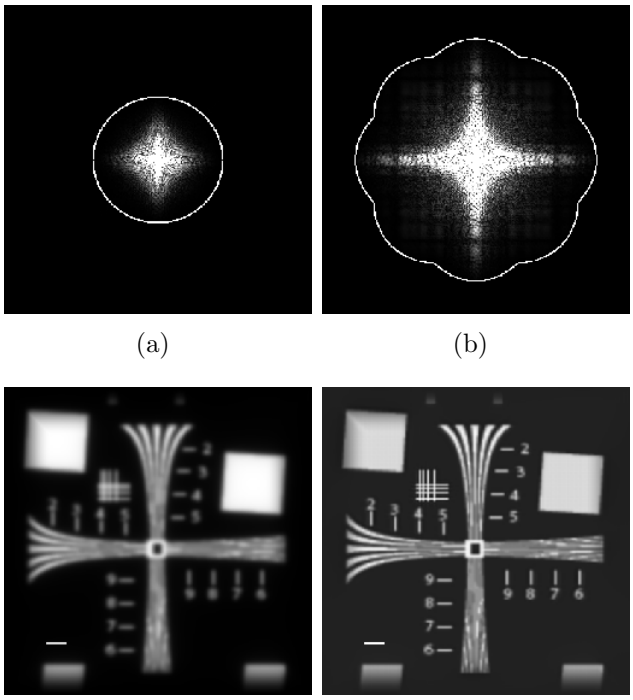

(a) (b)

(c) (d)

Figure 2.10: *Simulated data. (a) Simulation of a classical component. (c) The inverse Fourier transform of (a) represents an image from a classical wide-field microscope. (b) Reconstructed Fourier transform with enlarged area of detectable Fourier frequencies. (d) The inverse Fourier transform of (b) represents a reconstructed image with an improved resolution. Scale bar* 1 μm.

The resolution in the reconstructed image is improved along the direction collinear with the direction of the excitation pattern vector $\vec{\kappa}$ only. To obtain an isotropic extension of detectable frequencies, we need to take data for different orientations of the excitation pattern (e.g.. 0°, 45°, 90°, 135°) as shown in Fig. 2.8. The effect of the resolution improvement is demonstrated in Fig. 2.9. The whole reconstructed image is shown in Fig. 2.10.

2.6 Excitation pattern

We assume a situation where a coherent monochromatic beam (wavelength λ_{em}) hits a diffraction grating. Individual diffracted orders are focused on the back focal plane (BFP) of an objective. Passing through the objective the diffracted orders are transformed into planar waves. They propagate in a direction with a different

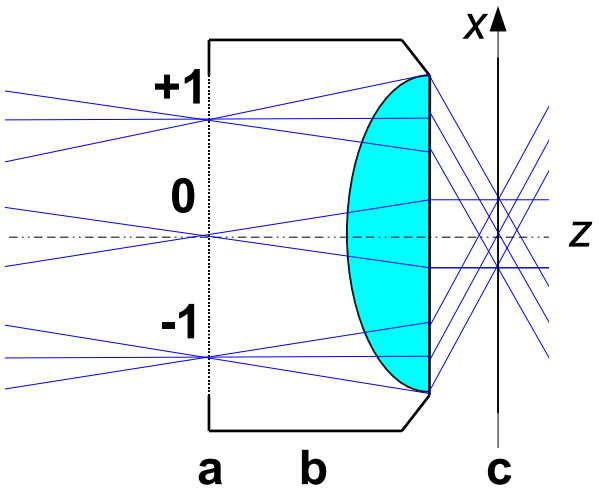

Figure 2.11: *Generation of the excitation pattern. Three diffracted beams (-1, 0, +1) are focused on the back focal plane (a) of the objective (b). They are transformed into plane waves. In the area of the overlap they interfere. In the sample plane (c) a harmonic interference pattern is created. The* x*-axis lies in the sample plane and* z*-axis is along the optical axis.*

angle with respect to the optical axis (see Fig. 2.11). The angle is determined by the position of the focused beam in the BFP.

Let $\vec{E}_m$, $(m = -1, 0, 1)$ be a real amplitude of the m^{th} diffracted order and $\vec{\kappa}_m$ and φ_m their wave vectors and phases, respectively ($\kappa_{-1}^2 = \kappa_{+1}^2 = \kappa_0^2 \equiv \kappa^2$, $\kappa = \frac{2\pi}{\lambda_{ex}}$; $\varphi_{-1} + \varphi_{+1} = \varphi_0$). The polarisation is in the direction of the y-axis (perpendicular to the plane of the figure).

We set the origin of a coordinate system to the intersection of a sample plane and the optical axis (z direction). The x axis is collinear with the direction of the displacement of the focused beams in the BFP (see Fig. 2.11). We selected only ± 1 and 0 diffracted orders. Corresponding plane waves have spatial frequencies:

$$\begin{aligned} \vec{\kappa}_{-1} &= (\kappa_x, 0, \kappa_z)\,, \\ \vec{\kappa}_0 &= (0, 0, \kappa)\,, \\ \vec{\kappa}_{+1} &= (-\kappa_x, 0, \kappa_z)\,. \end{aligned}$$

The electric field in the overlapping area of all three diffracted beams is given by:

$$\vec{E}\,(\vec{r}) = \vec{E}_{-1} e^{i(\vec{\kappa}_{-1}\cdot\vec{r}+\varphi_{-1})} + \vec{E}_0 e^{i(\vec{\kappa}_0\cdot\vec{r}+\varphi_0)} + \vec{E}_{+1} e^{i(\vec{\kappa}_{+1}\cdot\vec{r}+\varphi_{+1})}. \qquad (2.36)$$

The interference pattern is obtained as a square of the amplitude of the electric field:

$$I_{ex} \propto \vec{E} \cdot \overline{\vec{E}};$$

$$\begin{aligned} I_{ex}(\vec{r}) \propto & \left|\vec{E}_{-1}\right|^2 + \left|\vec{E}_0\right|^2 + \left|\vec{E}_{+1}\right|^2 + 2\vec{E}_{-1} \cdot \vec{E}_{+1} \cos\left(2\kappa_x x + \Delta\varphi_{-1,1}\right) + \\ & + 2\vec{E}_0 \cos\left(\left(\kappa - \kappa_z\right) z\right) \left[\vec{E}_{-1} \cos\left(\kappa_x x + \Delta\varphi_{-1,0}\right) + \vec{E}_{+1} \cos\left(\kappa_x x + \Delta\varphi_{0,1}\right)\right] + \\ & + 2\vec{E}_0 \sin\left(\left(\kappa - \kappa_z\right) z\right) \left[\vec{E}_{-1} \sin\left(\kappa_x x + \Delta\varphi_{-1,0}\right) - \vec{E}_{+1} \sin\left(\kappa_x x + \Delta\varphi_{0,1}\right)\right], \end{aligned} \tag{2.37}$$

where $\Delta\varphi_{k,l} = \varphi_k - \varphi_l$.

With the assumption $\left|\vec{E}_{-1}\right| = \left|\vec{E}_{+1}\right| \equiv \left|\vec{E}\right|$ (same power of diffraction orders[2]) and $\varphi_{-1} = \varphi_{+1} \equiv \varphi$ we can simplify Eq.2.37:

$$\begin{aligned} I_{ex}(\vec{r}) \propto & \left|\vec{E}_0\right|^2 + 2\left|\vec{E}\right|^2 \left(1 + \cos\left(2\kappa_x x\right)\right) + \\ & + 8\vec{E}_0 \cdot \vec{E} \cos\left(\varphi_0 - \varphi\right) \cos\left(\left(\kappa - \kappa_z\right) z\right) \cos\left(\kappa_x x\right). \end{aligned} \tag{2.38}$$

and the Fourier transform:

$$\begin{aligned} \tilde{I}_{ex}(\vec{k}) \propto & \left(\left|\vec{E}_0\right|^2 + 2\left|\vec{E}\right|^2\right) \delta_{[0,0,0]}(\vec{k}) + \left|\vec{E}\right|^2 \left(\delta_{[-2\kappa_x,0,0]}(\vec{k}) + \delta_{[2\kappa_x,0,0]}(\vec{k})\right) + \\ & + 2\vec{E}_0 \cdot \vec{E} \cos\left(\varphi_0 - \varphi\right) \left(\delta_{[-\kappa_x,0,\pm(\kappa-\kappa_z)]}(\vec{k}) + \delta_{[\kappa_x,0,\pm(\kappa-\kappa_z)]}(\vec{k})\right), \end{aligned} \tag{2.39}$$

where $\delta_{[\alpha,\beta,\gamma]}(\vec{k}) = \delta(k_x - \alpha,\, k_y - \beta,\, k_z - \gamma)$.

If we block the zero diffraction order $\left|\vec{E}_0\right| = 0$ we find a harmonic excitation pattern with a sinusoidal profile in the focal plane ($z = 0$) (compare with Eq.(2.13) on page 17)

$$I_{ex} \propto 2\left|\vec{E}\right|^2 \left(1 + \cos\left(2\kappa_x x\right)\right)$$

The Fourier transform

$$\tilde{I}_{ex}(\vec{k}) \propto 2\left|\vec{E}\right|^2 \left[\delta_{[0,0]}(\vec{k}) + \frac{1}{2}\left(\delta_{[-2\kappa_x,0]}(\vec{k}) + \delta_{[2\kappa_x,0]}(\vec{k})\right)\right]$$

consists of three δ peaks in positions 0 and $\pm 2\kappa_x$ on the k_x axis.

If we allow the zero diffraction order to interfere, we find a modified excitation pattern in the focal plane ($z = 0$). This consists of two cosine functions with different spatial frequencies:

$$\begin{aligned} I_{ex}(\vec{r}) \propto & \left|\vec{E}_0\right|^2 + 2\left|\vec{E}\right|^2 \left(1 + \cos\left(2\kappa_x x\right)\right) + \\ & + 8\vec{E}_0 \cdot \vec{E} \cos\left(\varphi_0 - \varphi\right) \cos\left(\kappa_x x\right). \end{aligned} \tag{2.40}$$

[2]This assumption cannot be used for blazed gratings.

The Fourier transform is

$$\tilde{I}_{ex}(\vec{k}) \propto \left(\left|\vec{E}_0\right|^2 + 2\left|\vec{E}\right|^2 \right) \delta_{[0,0]}(\vec{k}) + \left|\vec{E}\right|^2 \left(\delta_{[-2\kappa_x,0]}(\vec{k}) + \delta_{[2\kappa_x,0]}(\vec{k}) \right) + \\ + 2\vec{E}_0 \cdot \vec{E} \cos\left(\varphi_0 - \varphi\right) \left(\delta_{[-\kappa_x,0]}(\vec{k}) + \delta_{[\kappa_x,0]}(\vec{k}) \right). \tag{2.41}$$

It consist of five δ peaks in positions $\pm 2\kappa_x$, $\pm\kappa_x$ and 0 on the k_x axis. The Fourier transform of acquired data $\tilde{Im}^n$ (Eq.(2.20)) contains $M = 5$ components ($\tilde{\rho}_0$, $\tilde{\rho}_{\pm 1}$ and $\tilde{\rho}_{\pm 2}$) to separate:

$$\tilde{Im}^n(\vec{k}) = B_0\tilde{\rho}_0(\vec{k}) + B_{-1}e^{-i\left(2\frac{2\pi}{N}n+\phi_0\right)}\tilde{\rho}_{-1}(\vec{k}) + B_{+1}e^{i\left(2\frac{2\pi}{N}n+\phi_0\right)}\tilde{\rho}_{+1}(\vec{k}) \\ + B_{-2}e^{-i\left(\frac{2\pi}{N}n+\frac{\phi_0}{2}\right)}\tilde{\rho}_{-2}(\vec{k}) + B_{+2}e^{i\left(\frac{2\pi}{N}n+\frac{\phi_0}{2}\right)}\tilde{\rho}_{+2}(\vec{k}), \tag{2.42}$$

where B_m is the amplitude of the separated components. We have to acquire $N \geq 5$ images with different translations ($n\frac{p}{N}$, ($n = 1..N$), $p = \frac{2\pi}{2|\vec{\kappa}|}$) of the excitation pattern.

2.7 Concept of PEM in real space

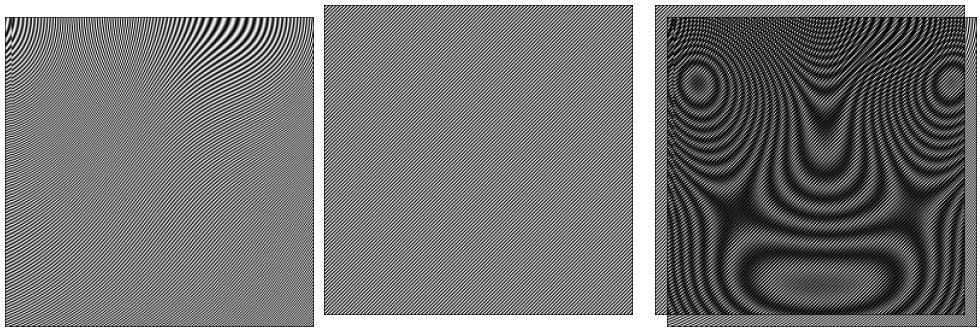

(a) (b) (c)

Figure 2.12: Demonstration of the moiré fringes. Two high-frequency patterns (a) - 'sample', (b) - 'excitation pattern' and their product (c) - 'detected image' (a low-frequency pattern).

The encoding of high spatial frequency information in the microscopic image acquired with a patterned excitation can be explained in real space through the moiré effect. A superposition (multiplication) of two periodic patterns $P_1 = \cos(k_1 x)$ and $P_2 = \cos(k_2 x)$ with spatial frequencies k_1 and k_2, respectively gives rise to a structure containing the sum and the difference of k_1 and k_2

$$P_1 P_2 = \frac{1}{2}\left[\cos\left((k_1 + k_2)x\right) + \cos\left((k_1 - k_2)x\right)\right]$$

This means that two high-frequency periodic patterns can produce a pattern with low-frequency (moiré) fringes ($k = k_1 - k_2$). If, for example, k_1 lies outside the OTF support ($k_1 > k_{cut}$) then the structure of P_1 cannot be resolved under a microscope. However, the multiplication of P_1 with a pattern P_2 of spatial frequency k_2 where $|k_1 - k_2| < k_{cut}$ can be resolved. If the pattern P_2 is known (excitation pattern) we can reconstruct the unknown unresolvable pattern P_1 (sample) from the recorded (resolvable) image P_1P_2 (patterned excitation of the fluorescent sample).

A complicated structure of biological samples can be decomposed (by the Fourier transform) into a sum (integral) of the sine and cosine functions (components) and then the moiré effect holds for each individual component. The moiré effect is demonstrated in Fig. 2.12.

3 Experimental setup

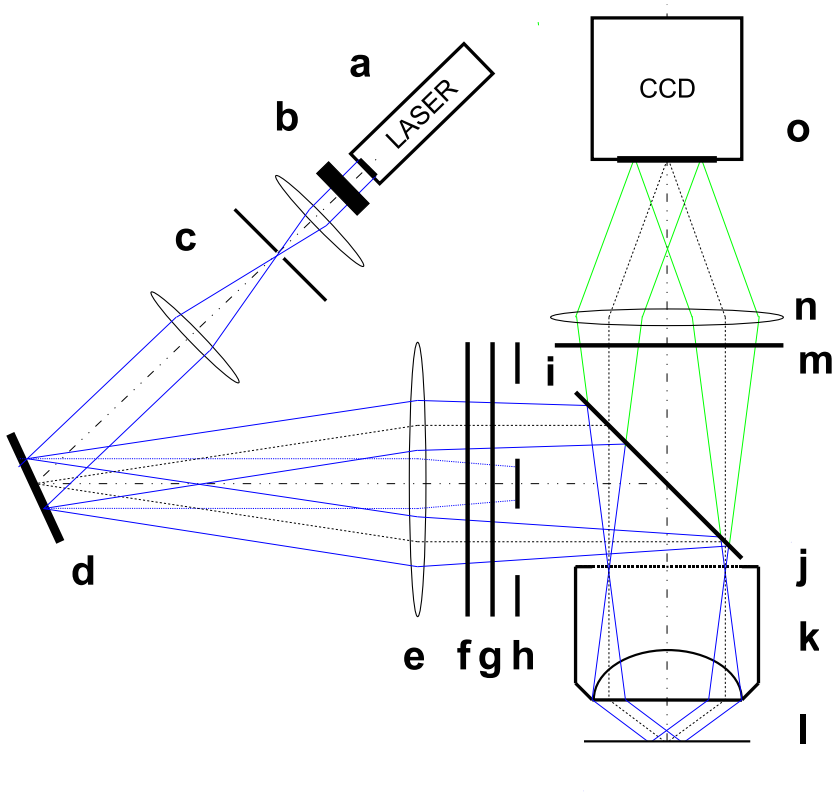

Figure 3.1: *Experimental setup. (a) Laser source, (b) shutter, (c) beam expander with a pinhole, (d) spatial light modulator (SLM), (e) focusing lens, (f) half-wave plate followed by (g) linear polarizer, (h) zero diffraction order block, (i) dichroic beam-splitter, (j) back focal plane of the objective, (k) objective, (l) sample plane, (m) emission filter, (n) tube lens, (o) CCD camera.*

Fig. 3.1 illustrates the experimental setup. The whole beam path was enclosed in tubes in order to avoid the air drafts.

3.1 Objective

An objective (Leica, Germany; 63×, 1.2NA, water immersion) was used for both illumination and detection (an epifluorescence setup). The z-position of the objective could be controlled by a piezo-driven focusing device (PIFOC P-725, Physik Instrumente, Germany; resolution 0.75 nm).

3.2 Illumination

A solid state laser was used as a coherent light source (mQ Lasersysteme, Germany; $\lambda_{ex} = 473\ nm$, nominal output power 50 mW). The laser beam was expanded by a beam expander consisting of two positive lenses (focal lengths $f_1 = 25\,\text{mm}$ and $f_2 = 500\,\text{mm}$). A pinhole ($10\,\mu m$) was inserted in the common focal plane of the two lenses to clean the beam. The beam was reflected on a high resolution spatial light modulator (SLM) (HOLOEYE HEO 1080 P, Holoeye Photonics, Germany; 1920×1080 pixels, 8 μm pixel pitch). A system based on reflective liquid crystal micro-displays. This device was used as a phase diffraction grating. A periodic pattern consisting of parallel stripes (a grid) with a desired grating period, position and orientation was displayed on the SLM. Separated diffracted orders were focused with a lens (focal length $f = 1\,m$) onto the back focal plane (BFP) of the objective. The zero diffraction order could be blocked with a black screen before the BFP. The polarisation was rotated by a half-wave plate to be collinear with the stripes of the diffraction grating. The half-wave plate was followed by a linear polarizer (rotated independently) to further 'clean up' the polarisation. (It was important as we needed to achieve a maximal modulation of the excitation pattern.) After passing through the objective lens the diffracted orders focused on the BFP were again transformed into individual plane waves. They passed through the sample plane under different angles with respect to the optical axis (see Fig. 2.11) and they created an interference pattern in the region of overlap. As the interference pattern in the sample plane is actually an image of the grid displayed on the SLM (selection of the ± 1 and 0 diffraction orders represents a filtering of spatial frequencies in the Fourier plane - compare with Fig. 1.7(a, b)) where the lateral position and the orientation of the grid displayed on the SLM determines the position and the orientation of the pattern in the image plane. The advantage of using the SLM instead of a physical grating is that no translation or rotation of the SLM device is required. Moreover, by optimising gray values of the displayed grid we can enhance the optical power guided into the diffracted orders. The characterization of the SLM device was carried out by Liisa Hirvonen.

3.3 Detection

Emitted light was collected by the objective and the tube lens (Leica, Germany; magnification $1\times$). A long pass filter was inserted into the detection path ($\lambda_{em} >$ 510 nm) and the image was recorded on a CCD camera (Imager Intense, La Vision, Germany; 12 bit, 1376×1040 pixels, 6.45 μm pixel-size).

3.4 Sampling

We used a diffraction grating (600 lines/mm) for the calibration of the magnification. From a magnified image of the grating we computed one pixel in the CCD camera

corresponds to 83.3 nm in the sample plane. The objective used in our setup (1.2 NA, water immersion) is capable of detecting spatial frequencies (in the focal plane) of up to $k_{cut} \doteq 15/\lambda_{em}$ (see Eq.(2.10)). To fulfill the Nyquist limit for $\lambda_{em} > 510$ nm, the minimal required sampling is

$$\Delta = \frac{1}{2}\frac{2\pi}{k_{cut}} = \frac{\lambda_{em}}{4\mathrm{NA}} = \ 107 \text{ nm}. \tag{3.1}$$

With the pixel-size of 83.3 nm, the recorded image was slightly oversampled.

4 Reconstruction Algorithm Description

The reconstruction algorithm follows the theory described in section 2.5. The program was written in MATLAB (The MathWorks, USA) using the image processing toolbox DIP*image* [33] (TU Delft, Netherlands).

Transformation between the metric system and the pixel units ($\vec{r}$[m] $\rightarrow \vec{r}$[pixels] in real space and $k[\mathrm{m}^{-1}] \rightarrow \vec{k}$[pixels] in Fourier space) in the image is computed with the transformation matrices $\mathbb{R}$, $\mathbb{K}$:

$$\mathbb{R} = \frac{M}{CCDpixelsize} \begin{pmatrix} 1 & 0 \\ 0 & 1 \end{pmatrix}, \mathbb{K} = \frac{CCDpixelsize}{M} \begin{pmatrix} \frac{S_x}{2\pi} & 0 \\ 0 & \frac{S_y}{2\pi} \end{pmatrix}; \tag{4.1}$$

$$\vec{r}[\text{pixels}] = \mathbb{R} \cdot \vec{r}[\text{m}] \text{ and } \vec{k}[\text{pixels}] = \mathbb{K} \cdot \vec{k}[\text{m}^{-1}], \tag{4.2}$$

where *CCDpixelsize* is the pixel-size of the CCD camera, M is the magnification of the system and $S_x \times S_y$ is the size of the image (in pixels).

4.1 Loading Images

Fourier transforms of the recorded images for different orientations and positions of the pattern are loaded into an array structure. The DIP*image* structure "*imar*" allows to treat the individual images as elements of a vector (see Eq.(2.21)).

4.2 PSF Simulation

The *PSF* is computed from the parameters of the objective and the camera using the program *"ksimPSF"* written by Rainer Heintzmann. The program is based on the vectorial high-NA theory [31], [30]. The *OTF* is obtained as the Fourier transform of the *PSF*.

An experimental *PSF* can be used as an option. We took an image of fluorescent beads (diameter 100 nm) and selected one individual bead. The image of the bead can be optionally made symmetric by a radial averaging.

4.3 Intensity Offset Subtraction

The global offset is subtracted from raw data. The offset is estimated from a dark image taken with the same setting of the camera (integration time) as the measured images but with closed laser shutters.

4.4 Image Alignment and Brightness Correction

During the acquisition of the images a lateral drift of the sample can be present. Time between the acquisition of the images for different orientations of the grating can be considerably long and vibration or translation of the sample stage results in

a slight shift of the sample. This can severely deteriorate the results. Therefore, precise alignment of the acquired images is vital. The algorithm for alignment is based on a cross-correlation method. Sharp borders of the recorded images might cause difficulties in the cross-correlation based estimation of the drift. The edges of all images are therefore dimmed down using a window function (a Hann window with a flat central area).

4.4.1 Alignment for images with different orientations of the grating

We compute a sum of images over all positions ($n = 1..N$) of the excitation pattern for one orientation α_i of the pattern:

$$Im_{\mathrm{SUM}}^{\alpha_i} = \sum_{n=1}^{\mathrm{N}} Im_n^{\alpha_i}. \tag{4.3}$$

The drift of the sample between the different pattern orientations α_j is estimated from the position of the peak in the cross-correlations of $Im_{\mathrm{SUM}}^{\alpha_i}$ and $Im_{\mathrm{SUM}}^{\alpha_j}$.

4.4.2 Alignment for images with different position of the grating within one orientation

The drift of the sample between the individual shifts of the pattern (within one orientation) is a difficult task and it is hard to compensate for. The cross-correlation method cannot be used directly due to the projected pattern. Images must be processed with various Fourier filters prior to the drift estimation. Tests on the simulated data revealed that this correction is not always successful and must be used with care.

4.4.3 Brightness correction

Correction for the fluctuation of the fluorescent light intensity (e.g. due to the instability of the laser source or the polarisation of the fluorophores in the sample) between the individual orientations of the pattern α_j; $j = 1..D$ is also estimated from the $Im_{\mathrm{SUM}}^{\alpha_j}$ (Eq.(4.3)). A large bright area Ω is determined in the average image over the orientations of the pattern

$$Im_{\mathrm{SUM}}^{\mathrm{AVG}} = \frac{1}{D} \sum_{j=1}^{D} Im_{\mathrm{SUM}}^{\alpha_j}$$

using the DIP*image* function *"threshold"* (Isodata algorithm). The individual images $Im_n^{\alpha_j}$ for different orientations of the pattern are corrected such that $Im_{\mathrm{SUM}}^{\alpha_j} = Im_{\mathrm{SUM}}^{\mathrm{AVG}}$ over the area Ω. Correction for the intensity fluctuation between the individual positions of the pattern (within one pattern orientation) is described in section 4.5.

4.5 Separation Matrix Optimization

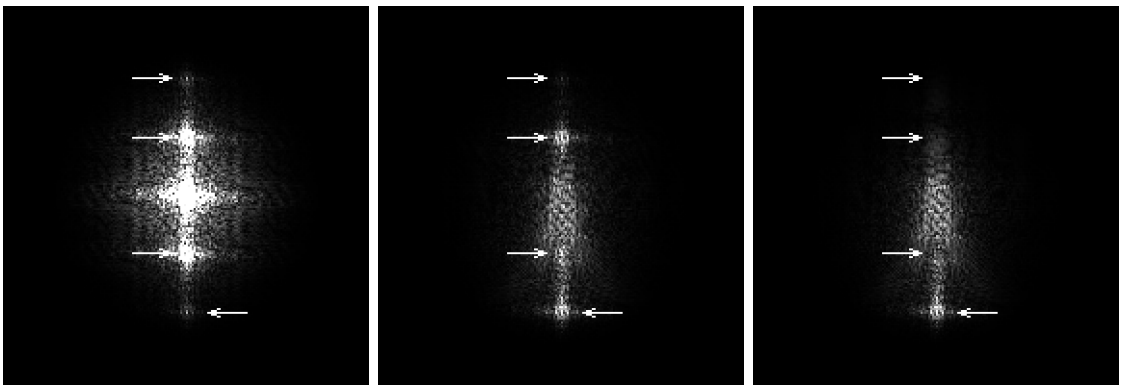

(a) (b) (c)

Figure 4.1: *Simulated data. Demonstration of the separation matrix correction for data taken with the modified excitation pattern Eq.*(2.40). *A random error in the precise translation of the excitation pattern was introduced in the simulation. The maximum inaccuracy of the translation was about 2% of the precise value* $2\pi/N$ *(see Eq.2.20). (a) The Fourier transform of raw data. Five components to separate are present in the figure. White arrows heading right point at -2, -1 and +1 components. The arrow heading left point at +2 component. (b) Separated +2 component without the correction of the separation matrix. -2, -1 and +1 components are mixed in the +2 component. (c) +2 component after the correction of the separation matrix.*

The separation matrix and its inversion are computed according to Eq.(2.23). Imprecision and imperfection of the experimental setup, namely:

- imprecise shift of the grating
- fluctuation of the excitation light intensity between individual images
- bleaching of the pattern into the sample

have large influence on the quality of separation. To a certain extent, this hardware inaccuracy can be corrected computationally by optimising the matrix $\mathbb{A}$ in Eq.(2.24).

If the steps of the pattern shift are not precise (steps in Eq.(2.19) are not exactly $\frac{p}{N}$) and (or) if the intensity of the excitation light significantly fluctuates, the components mix together. We can observe several unwanted peaks in each of the separated components (see Fig. 4.1). This generates artefacts in the reconstructed image. To achieve better separation we can iteratively optimize the separation matrix $\mathbb{A}$ by varying the phase $\Delta\phi$ and (or) the intensity ΔI of individual elements:

$$A'_{nm} = (1 + \Delta I_m) \exp\left\{ i\frac{2\pi}{N}(n-1)\left[(m-1) - \frac{M-1}{2} + \Delta\phi_m\right]\right\}, \tag{4.4}$$

with ($n = 1..N$, $m = 1..M$). By adjusting the phase $\Delta\phi$ and (or) the intensity ΔI, we are try to minimize the 'similarity' between the two separated (non-shifted) components such that there is no mixing of one in another. This means in a cross-correlation between two separated components

$$c_{ij}^{(0)}(\vec{k}) = \iiint\limits_{\text{k-space}} d\vec{k}' \ \tilde{\rho}_i(\vec{k}')\overline{\tilde{\rho}_j}(\vec{k}' + \vec{k}) \equiv \{\tilde{\rho}_i \star \tilde{\rho}_j\}(\vec{k})$$

we want to minimize the magnitude of the central pixel ($\vec{k} = 0$) for $i \neq j$:

$$\begin{aligned} c_{ij}^{(0)}(0) &= \left\{ \left(\mathbb{A}'^{-1} \cdot \vec{\tilde{I}m} \right)_i \star \left(\overline{\mathbb{A}'^{-1} \cdot \vec{\tilde{I}m}} \right)_j \right\}(0) \\ &= \iiint\limits_{\text{k-space}} d\vec{k}' \left(\sum_{p=1}^{N} A'^{-1}_{ip} \tilde{Im}_p(\vec{k}') \right) \left(\overline{\sum_{q=1}^{N} A'^{-1}_{jq} \tilde{Im}_q(\vec{k}')} \right), \end{aligned} \tag{4.5}$$

where we used Eq.(2.24). Lines above variables denotes the complex conjugation and the integration is over the whole Fourier transform of the image. Additionally, we can do a similar operation with the shifted components $\tilde{\rho}_i^{shift}$ from Eq.(2.25). Perfectly separated components should have a maximum amplitude of the complex value

$$c_{ij}^{(2\vec{\kappa})}(0) = \left\{ \tilde{\rho}_i^{shift} \star \tilde{\rho}_j^{shift} \right\}(0) \tag{4.6}$$

for neighboring orders $i = j \pm 1$, as they should contain the same information within the region of overlap.

Minimizing $c_{ij}^{(0)}(0)$ and maximizing $c_{ij}^{(2\vec{\kappa})}(0)$ requires separation and a cross-correlation in every step of the iterative optimization. This can be very time consuming especially for large images. The method can be significantly sped up [28]. Rewriting Eq.(4.5)

$$\begin{aligned} c_{ij}^{(0)}(0) &= \sum_{p=1}^{N} \sum_{q=1}^{N} A'^{-1}_{ip} \overline{A'^{-1}_{jq}} \iiint\limits_{\text{k-space}} d\vec{k}' \ \tilde{Im}_p(\vec{k}') \overline{\tilde{Im}_q(\vec{k}')}, \\ &= \sum_{p=1}^{N} \sum_{q=1}^{N} A'^{-1}_{ip} \overline{A'^{-1}_{jq}} D_{pq}^{(0)}, \end{aligned} \tag{4.7}$$

where $D_{pq}^{(0)} = \iiint\limits_{\text{k-space}} d\vec{k}' \ \tilde{Im}_p(\vec{k}') \overline{\tilde{Im}_q(\vec{k}')}$ is the value of the center pixel ($\vec{k} = 0$) of the cross-correlation between the Fourier transforms of the acquired images. Eq.(4.7)

can be rearranged

$$\begin{aligned} c_{ij}^{(0)}(0) =& \sum_{p=1}^{N}\sum_{q=1}^{N} A'^{-1}_{ip}\overline{A'^{-1}_{jq}}D_{pq}^{(0)} \\ =& \sum_{p=1}^{N}\sum_{q=1}^{N} A'^{-1}_{ip}D_{pq}^{(0)}\left(\overline{A'^{-1}_{qj}}\right)^{\mathrm{T}} \\ =& \mathbb{A}'^{-1}\cdot\mathbb{D}^{(0)}\cdot\left(\mathbb{A}'^{-1}\right)^{+}. \end{aligned} \tag{4.8}$$

Symbol + denotes the Hermitian conjugation. Similarly the cross-correlation between the shifted components:

$$c_{ij}^{(2\vec{\kappa})}(0) = \mathbb{A}'^{-1}\cdot\mathbb{D}^{(2\vec{\kappa})}\cdot\left(\mathbb{A}'^{-1}\right)^{+}, \tag{4.9}$$

where $D_{pq}^{(2\vec{\kappa})} = \iiint\limits_{\mathrm{k-space}} d\vec{k}'\ \tilde{Im}_p(\vec{k}')\overline{\tilde{Im}_q(\vec{k}'-(q-p)2\vec{\kappa})}$.

Correlation matrices $\mathbb{D}^{(0)}$ and $\mathbb{D}^{(2\vec{\kappa})}$ do not change during the iterative procedure. They have to be computed only once in the beginning and the iterative procedure is much faster then. The computation for the correlation matrix $\mathbb{D}^{(2\vec{\kappa})}$ can be further sped up by restricting the images only to the area of the mutual overlap of the separated components.

Correction for bleaching of the pattern into the sample is difficult. The procedure described above can slightly compensate for this imperfection of the acquired images but the result is usually severely deteriorated with residual pattern and artefacts. An analysis of artefacts in the structured illumination methods although in a different context can be found in [29].

4.6 Separation of Components

Components $\vec{\tilde{\rho}}$ are obtained according to Eq.(2.24) using the corrected (section 4.5) matrix $\mathbb{A}$ and the corrected (section 4.4) Fourier-transformed images $\vec{\tilde{Im}}$.

4.7 Mutual Shift Determination Between the Separated Components

The mutual shift of the separated components (which corresponds to the spatial frequency of the pattern $2\vec{\kappa}$) is estimated with sub-pixel precision using the function *"findshift"* (see Appendix B). Input values are the separated zero order component $\tilde{\rho}_0$ and one of the side-shifted components $\tilde{\rho}_{\pm 1}$. If more components are present (e.g. if we do not block the zero diffracted order - see Eq.(2.40)), we can determine the mutual shift in several ways. We can estimate the shift $\vec{P}_m$ ($m = 1..\frac{M-1}{2}$) of each side component

1. independently for the neighboring components
2. from the first component only (shift $\vec{P}_1$). We estimate the shift of the second (or higher m-th) component as the integer multiplication of the value for the first component $\vec{P}_m = m\vec{P}_1$.
3. from the second component only (shift $\vec{P}_2$) from the cross-correlation of the zero and the second component. We set the position of the first component as a half of it: $\vec{P}_1 = \frac{1}{2}\vec{P}_2$.

By default, we use the second option but in some situation the others can be used (e.g.. misalignment of the experimental setup such as if the illumination pattern is tilted with respect to the focal plane).

4.8 Correction for the Initial Phase of the Pattern

The initial phase ϕ_0 (see Eq.(2.16) and Eq.(2.17)) is estimated as the phase of the complex value $c_{ij}^{(2\vec{\kappa})}(0)$ for neighboring components $i = j + 1$ (see Eq.(4.6)). The ideally separated components

$$\tilde{\rho}_0^{shift}(\vec{k}) = \left|\tilde{\rho}_0^{shift}(\vec{k})\right| e^{i\theta_0(\vec{k})}$$
$$\tilde{\rho}_{+1}^{shift}(\vec{k}) = \left|\tilde{\rho}_{+1}^{shift}(\vec{k})\right| e^{i(\theta_{+1}(\vec{k})+\phi_0)}$$

contain exactly the same information about the phase of the Fourier transform within the area of the overlap:

$$e^{i\theta_0(\vec{k})} = e^{i\theta_{+1}(\vec{k})}.$$

Then

$$c_{01}^{(2\vec{\kappa})}(0) = \left|\tilde{\rho}_0^{shift}\right| \left|\tilde{\rho}_1^{shift}\right| e^{-i\phi_0}$$

and the initial phase

$$\phi_0 = \arctan \frac{\Im\left(c_{01}^{(2\vec{\kappa})}(0)\right)}{\Re\left(c_{01}^{(2\vec{\kappa})}(0)\right)}$$

where $\Re$ and $\Im$ denotes the real and imaginary part of $c_{01}^{(2\vec{\kappa})}(0)$, respectively.

4.9 Shift of the Components

The separated components are shifted back by the estimated value $\vec{P}$ such as their 'true' zero frequency is placed back to the origin and are corrected for the initial phase ϕ_0. If the recorded image were sampled correctly, the cut-off frequency border of the OTF is close to the edge of the $\tilde{Im}$. Therefore a resamplig by zero padding in the Fourier transform is needed to obtain space for the shift of the separated components.

We can slightly oversample the final image for smoother visual appearance of the reconstructed image.

The shift of the components by the value $\vec{P}$ (with the sub-pixel precision) is achieved through the multiplication by a phase gradient in reciprocal (in this case real) space (see Appendix A Eq.(A.7)).

4.10 Weighted Recombination of the Shifted Components

The shifted and ϕ_0 - corrected components are combined together with a pixel-wise weighting. A Wiener filter approach (Eq.(2.26)) is used to reduce artefacts which stem from noise [14].

All separated components are treated in individual non-resampled images throughout the reconstruction. Even the weights are computed with respect to these 'unprocessed' images. The final shifting my multiplication is the very last step, even after apodization. This reduces artefacts in the reconstructed image [14].

4.11 Apodization Function

An apodization function (2D - in plane) is generated according to Eq.(2.33) or Eq.(2.34). The value of $\frac{|\vec{k}|}{k_{cut}^{final}}(\vec{\sigma})$ in Eq.(2.33) and Eq.(2.34) is estimated from the relative distance of the point $\vec{k}$ from the border of the footprint of the reconstructed support (Euclidean distance transform).

4.12 Final Result

The final reconstructed image is computed as the inverse Fourier transformation of $\tilde{\rho}^{final}$ (see Eq.(2.35)).

5 Results and Discussion

5.1 Simulations

The algorithm for image reconstruction was optimized and tested on the simulated data. All data presented in this section are simulations for the water immersion objective (NA = 1.2, $n = 1.33$) and for the emission wavelength $\lambda_{em} = 510$ nm to be consistent with our experimental setup (see section 3). We used ideal simulated data (noise free, no drift, no brightness changes between the individual images, a precise shift of the pattern) as well as simulated data with additionally introduced imprecision.

We used a simulated image of beads (dots in random positions in the image) to quantify the resolution improvement. We measured the intensity profile FWHM (Full Width at Half Maximum) of the selected beads in the reconstructed and wide-field image. Every image of the bead was radially averaged, normalized to one at the maximum and fitted with a Gaussian curve

$$g(x) = \exp\left(-\frac{x^2}{2\sigma^2}\right) \tag{5.1}$$

The FWHM was computed from the parameter σ:

$$\mathrm{FWHM} = 2\sigma\sqrt{2\ln 2} \tag{5.2}$$

5.1.1 Effect of the apodization function

Apodization Function	$h^{\cos}_{goal}$	$h^{0.5}_{goal}$	$h^{1.2}_{goal}$	$h^{2.0}_{goal}$	WF	Theo
FWHM [nm]	101 ± 1	90 ± 1	111 ± 1	135 ± 2	238 ± 7	239

Table 5.1: *FWHM of the average intensity profile of the reconstructed simulated beads. The excitation pattern with a grating period of 271 nm was used. Four different apodization functions were used.* WF - *measured classical wide-field image from the simulated data.* Theo - *the theoretical wide-field image.*

The effect of the apodization function on the profile of the reconstructed image is demonstrated in Fig. 5.1. We simulated noise-free data for an excitation pattern with a grating period of 271 nm. This corresponds to the position of the δ peak in a distance of 78% of the k_{cut} border (Eq.(2.10)) and therefore results in 1.78× enlargement of the OTF support along every orientation of the excitation pattern.

Images of simulated beads were reconstructed using the apodization function $h^{\cos}_{goal}$ with a cosine profile computed according to Eq.(2.33) and the apodization functions h^{q}_{goal} computed from Eq.(2.34) for parameters $q = 0.5$, 1.2 and 2.0. Profiles of such apodization functions are shown in Fig. 2.7 on page 24.

Five individual beads were selected in every reconstructed image and their intensity was normalized to 1 at their maximum. We measured the FWHM of the

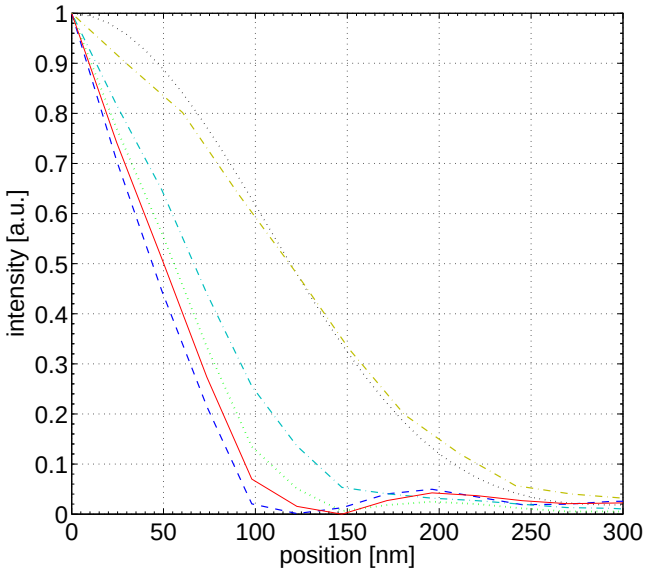

Figure 5.1: *Reconstruction of simulated (ideal) data. Average profiles (made radially symmetric) of reconstructed beads for different h_{goal} apodization functions. The profiles are stretched from 0 to 1. An excitation pattern with a grating period of 271 nm was used. The use of the apodization function with a cosine shape $h^{\cos}_{goal}$ (Eq.*(2.33)*) results in the bead profile plotted with the red solid line (*FWHM $= (101 \pm 1)$ nm*). Use of the apodization functions h^{q}_{goal} computed according to Eq.*(2.34) *for $q = 0.5$ results in the profile plotted with the blue dashed line (*FWHM $= (90 \pm 1)$ nm*), $q = 1.2$ in a green dotted line (*FWHM $= (111 \pm 1)$ nm*) and $q = 2$ in a cyan dot-and-dash line (*FWHM $= (136 \pm 2)$ nm*). The profile from a wide-field image is plotted with the yellow dashed line (*FWHM $= (238 \pm 7)$ nm*) and the theoretical profile is in a black dot line (*FWHM $= 239$ nm*).*

intensity profile (Eq.(5.2)). As the reconstruction of the noise-free simulated data exhibits very narrow distribution of the bead size, five selected beads was a sufficient set for the measurement. Average intensity profiles for different apodization functions used in the reconstruction are shown in Fig. 5.1 and the computed average FWHMs are in Table 5.1. The error was estimated as a standard deviation from the set of the measured individual FWHMs.

Fig. 5.1 shows that the apodization function can significantly change the shape of the reconstructed profile of the beads. Use of the apodization function $h^{\cos}_{goal}$ with the sinusoidal profile (Eq.(2.33)) and h^{q}_{goal} (Eq.(2.34)) for $q < 1.2$ results in ringing artefacts (see Fig. 5.1(a) the red, green and blue lines). On the other hand, use of the apodization function h^{q}_{goal} for $q > 1$ sacrifices the high Fourier frequencies and leads to the broadening of the profile (Fig. 5.1(a) the cyan line). The ringing artefacts can be also reduced by an appropriate value of the Wiener parameter γ in the weighted

averaging (see Eq.(2.31) on page 23).

It is difficult to compare the FWHM of the reconstructed profile with the FWHM of the classical wide-field image profile. The excitation patter with the grating period 271 nm allows to reconstruct 1.78 times higher Fourier frequencies. However, the use of the sinusoidal apodization function $h^{\cos}_{goal}$ results in the ca. 2.4 times smaller FWHM of the reconstructed profile if compared with the classical wide-field profile (see Table 5.1). This effect is due to the enhancement of high Fourier frequencies. The apodization function h^{q}_{goal} for $q = 2$ resembles the classical OTF (see Fig. 2.7) and indeed, the FWHM of the reconstructed bead is 1.76 times smaller (Table 5.1) if 1.78 times higher Fourier frequencies were reconstructed.

5.1.2 Effect of the grating period of the excitation pattern

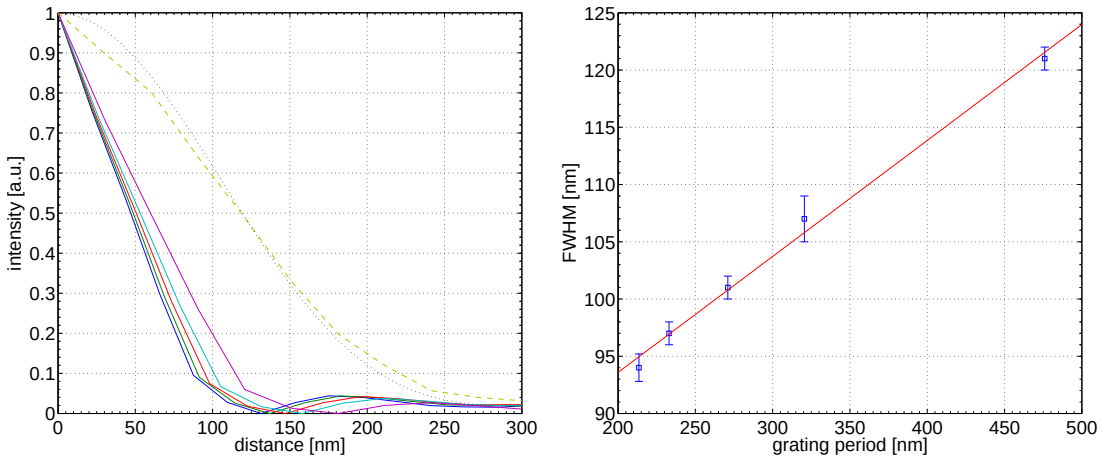

(a) (b)

Figure 5.2: *Reconstruction of the simulated data. (a) Intensity profiles (stretched form 0 to 1) of radially averaged beads from the reconstructed image. The data were simulated for a grating period of the pattern 213 nm (blue), 233 nm (green), 271 nm (red), 320 nm (cyan) and 476 nm (magenta). The radially averaged profile of the wide-field image of the bead is plotted with the yellow dashed line, the theoretical PSF in the black dotted line. (b) The linear relationship between the measured FWHMs of the reconstructed bead profile and the grating period of the excitation pattern.*

The dependence of the reconstructed bead size (FWHM of the radially averaged profile) on the grating period of the excitation pattern is demonstrated in Fig. 5.2. We used five different values of the grating period. The measured FWHM are shown in Table 5.2. The FWHM of the reconstructed image is linearly dependent on the grating period (Fig. 5.2(b)) as the maximal detected frequency, and thus the extension of the OTF support is linearly proportional to it.

grating period [nm]	213	233	271	320	476	WF
$2\left\|\vec{\kappa}\right\|/k_{cut}$ [%]	99	91	78	66	45	-
FWHM [nm]	94 ± 1	97 ± 1	101 ± 1	107 ± 2	121 ± 1	238 ± 7

Table 5.2: *FWHM of the average intensity profile of the reconstructed simulated beads. Five excitation patterns of different spatial frequencies were used in simulations. The apodization function with a sinusoidal profile* $h_{goal}^{\cos}$ *was used in the reconstruction.* $2\vec{\kappa}/k_{cut}$ *- the relative position of the* δ *peak in the image with respect to the cut-off border.* WF *- the measured classical wide-field image from the simulated data.*

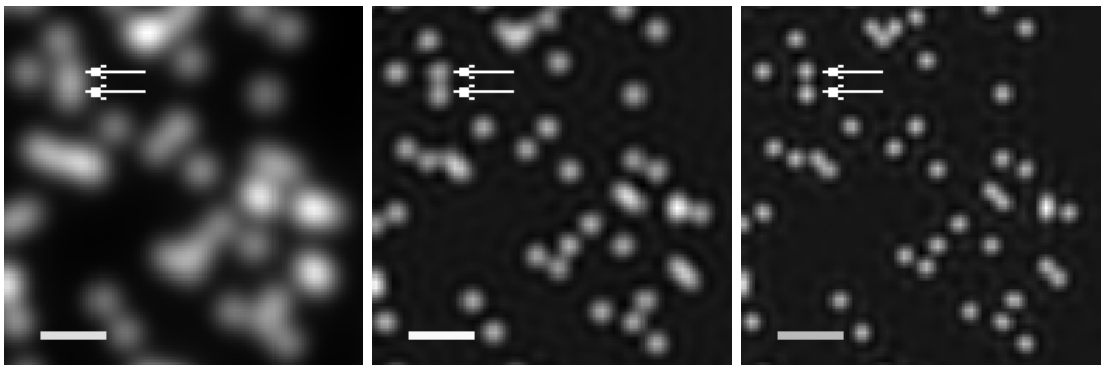

(a) (b) (c)

Figure 5.3: *Reconstruction of the simulated data. A detail of the reconstructed image of simulated fluorescent beads. (a) The classical wide-field image. (b, c) The reconstructed images for data with a grating-period (b) 476 nm and (c) 213 nm of the excitation pattern. Arrows point at two beads separated by ca. 150 nm. Scale bar 500 nm.*

There is a detail of the reconstructed image of the simulated fluorescent beads shown in Fig. 5.3. The reconstructed image was oversampled by a factor of 2.4. In the wide-field image Fig. 5.3(a), the individual beads are unresolved. We can barely resolve the two individual beads spaced close together (approximately 150 nm) in the reconstructed image (Fig. 5.3(b)) for the data with the grating period of 476 nm of the excitation pattern (1.45 times enlargement of the OTF support). However, if the pattern with the grating period of 213 nm was used (1.99 times enlargement of the OTF support), the beads are clearly resolved as two individual objects (Fig. 5.3(c)).

5.1.3 Effect of the Wiener parameter in noisy data

We made reconstruction for data with four different levels of the Poisson noise (a maximum 100, 500, 1000 and 5000 of the detected photons in one pixel). We used an excitation pattern with a 271 nm grating-period. Typical artefacts in the dark areas of the reconstructed images are shown in Fig. 5.4. No Wiener filter approach

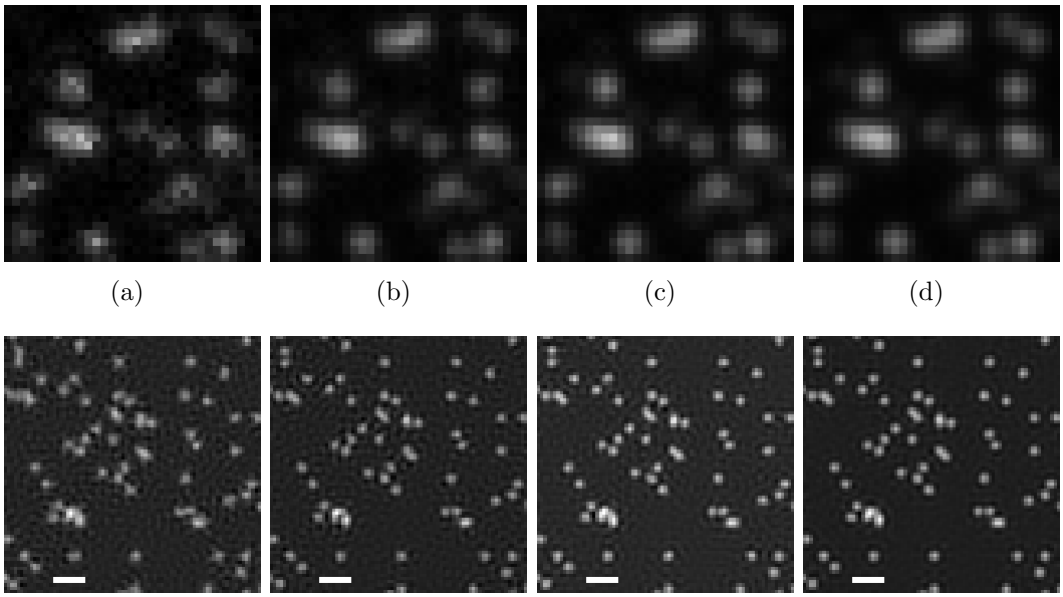

(a) (b) (c) (d)

(e) (f) (g) (h)

Figure 5.4: *Reconstruction of the simulated data. A detail of the reconstructed image of the simulated fluorescent beads for different Noise levels. No Wiener filter used ($\gamma = 0$) in (see Eq.*(2.26)*). (a-d) A detail of raw data with a Poisson Noise with maximum detected photons in 1 pixel (a) 100 photons, (b) 500 photons, (c) 1000 photons and (d) 5000 photons. (e-h) The reconstructed images from the data above (a different area and a scale shown). The residual artefacts are visible in the reconstruction of the noisy images. Scale bar 500 nm.*

was used for the reconstruction ($\gamma = 0$ in Eq.(2.26)).

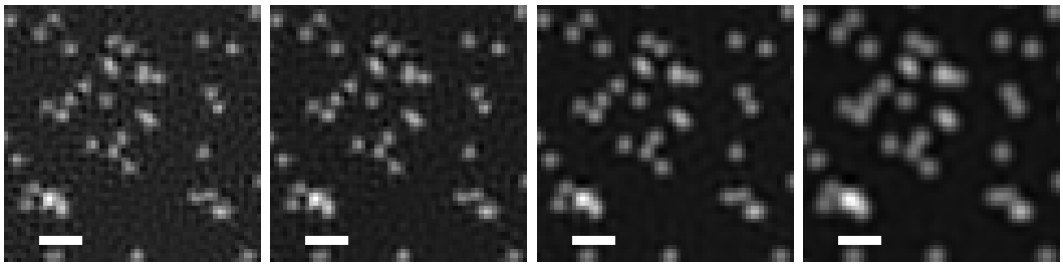

(a) (b) (c) (d)

Figure 5.5: *Reconstruction of the simulated data. A detail of the reconstructed image of the simulated fluorescent beads. Poisson noise with a maximum of 100 expected photons was added. Different parameters of the Wiener filter (see Eq.*(2.26)*) were used for the reconstruction. (a) No Wiener filter used ($\gamma = 0$). (b) $\gamma = 10^{-4}$ (c) $\gamma = 10^{-2}$ (d) $\gamma = 10^{-1}$. Scale bar 500 nm.*

The artefacts which stem from the noise can be reduced if a Wiener filter is used

in the weighted averaging (Eq.(2.31)). A demonstration of the artefacts reduction is in Fig. 5.5. Simulated data with a 271 nm grating period of the pattern and Poisson noise with 100 expected photons in one pixel were reconstructed for different values of the Wiener parameter γ in Eq.(2.31). The $h^{\cos}_{goal}$ apodization function was used. The reduction of the artefacts in the dark area is evident. However, we have to sacrifice the resolution as shown in Fig. 5.6 and in Table 5.3.

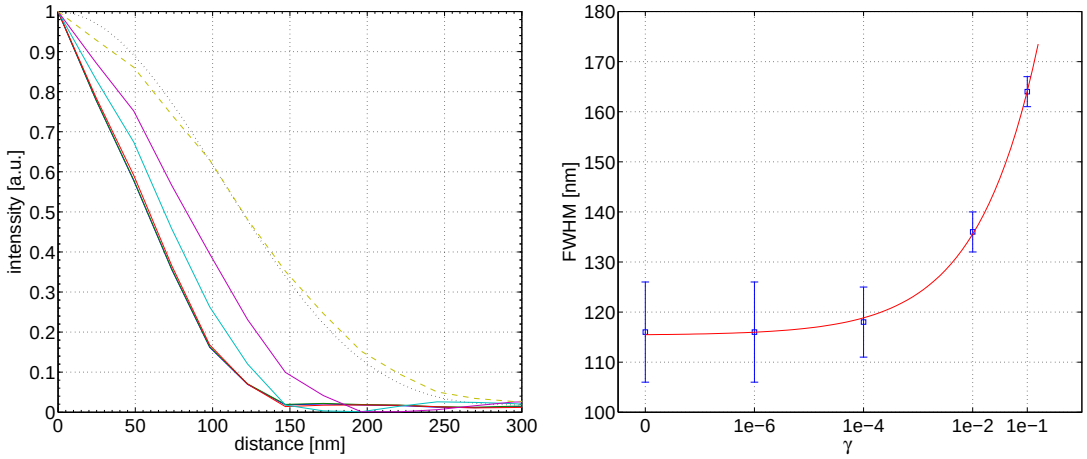

(a) (b)

Figure 5.6: *Reconstruction of the simulated data. Poisson noise with 100 expected photons in one pixel used in the simulations. The $h^{\cos}_{goal}$ apodization function was used. (a) Intensity profiles (stretched form 0 to 1) of the radially averaged simulated beads. Different Wiener parameters γ in Eq.*(2.26) *were used in the reconstruction. The profile for $\gamma = 0$ is plotted with the blue line, $\gamma = 10^{-6}$ in the green line, $\gamma = 10^{-4}$ in the red line (the blue, green and red line are almost indistinguishable from each other). $\gamma = 10^{-2}$ in the cyan line and $\gamma = 10^{-1}$ in the magenta line. The profile of the wide-field image is plotted with the yellow dashed line and the theoretical profile (PSF) in the black dotted line. (b) FWHM of the reconstructed beads as a function of Wiener parameters γ used in the reconstruction. The fit with an exponential curve is plotted with the red solid line.*

γ	0	10^{-6}	10^{-4}	10^{-2}	10^{-1}	WF
FWHM	116 ± 10	116 ± 10	118 ± 7	136 ± 4	164 ± 3	238 ± 26

Table 5.3: *FWHM of the average intensity profile of the reconstructed simulated beads. Five different Wiener parameters γ in Eq.*(2.26) *used in the reconstruction. The $h^{\cos}_{goal}$ apodization function was used. WF - the classical wide-field profile.*

The Wiener parameter $\gamma > 10^{-4}$ significantly widen the profile of the reconstructed beads (Fig. 5.6). We found the use of the apodization function $h^{\cos}_{goal}$ with

the Wiener parameter set to $\gamma = 10^{-4}$ as optimal combination in the reconstruction.

5.2 Real samples

5.2.1 Data acquisition

Data were acquired on the setup described in section 3 on page 31, Fig. 3.1. Four orientations of the pattern (0°, 45°, 90° and 135°) were projected on the sample. Three or five images (depending on the pattern) with different shift of the pattern (an integer number of pixels on the SLM) were recorded for every orientation of the grating. Synchronization between the shutter, SLM, half-wave plate, polarizer, PIFOC and the CCD camera was controlled with a software written by Liisa Hirvonen.

Adjustment of the objective (with the correction collar) to the right thickness of the cover slip was of great importance. An incorrect setting gives rise to the aberrations and largely deteriorates the contrast of the pattern in the recorded images.

5.2.2 Fluorescent beads

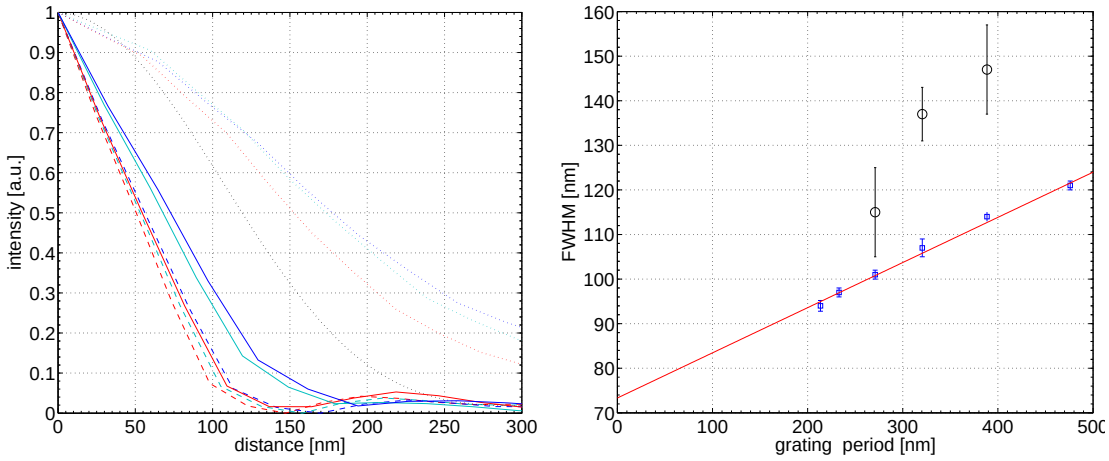

(a) (b)

Figure 5.7: *A comparison of the experimental (100 nm fluorescent beads) and the simulated data. (a) Profiles (stretched from 0 to 1) of the radially averaged images of fluorescent beads. The experimental data plotted with the solid lines, the simulated data plotted with the dashed lines and the wide-field experimental profiles in the dotted lines. The excitation pattern with grating period of 271 nm (red lines), 320 nm (cyan lines) and 389 nm (blue lines). The theoretical wide-field profile plotted with the black dotted line. (b) The comparison of the measured FWHM (black circles) with the simulated data (blue boxes).*

grating period [nm]	271	320	389
$\mathrm{FWHM_{exp}}$	115 ± 10	137 ± 6	147 ± 10
$\mathrm{FWHM_{sim}}$	101 ± 1	107 ± 2	114 ± 1
$\mathrm{FWHM_{exp}^{WF}}$	315 ± 12	366 ± 36	382 ± 20
$\mathrm{FWHM_{sim}^{WF}}$	236 ± 4	238 ± 8	232 ± 0

Table 5.4: *A comparison between experimental and simulated reconstructed data.* $\mathrm{FWHM_{exp}}$ *is for the reconstructed images,* $\mathrm{FWHM_{sim}}$ *for the simulated images,* $\mathrm{FWHM_{exp}^{WF}}$ *for the classical wide-field profile of experimental data,* $\mathrm{FWHM_{sim}^{WF}}$ *for the classical wide-field profile of simulated data. The theoretical value of* $\mathrm{FWHM^{WF}} = 238\,\mathrm{nm}$.

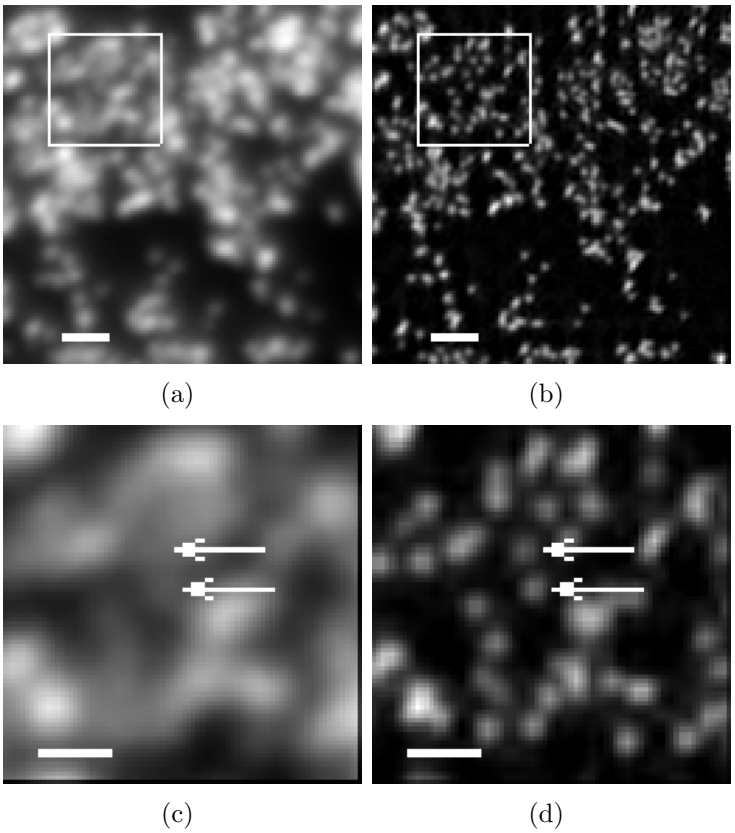

Figure 5.8: *Experimental data. Reconstructed images of 100 nm fluorescent beads (detail). (a) The classical wide-field image. (b) The reconstructed image for data acquired with a grating period of 320 nm of the excitation pattern. (c) and (d) show a detail of the wide-field and the reconstructed image, respectively. Arrows point at two beads separated approximately 250 nm. Scale bar (a, c)* 1 μm, *(b, d)* 500 nm.

We used fluorescent beads (L-5655) with 100 nm in diameter as a test sample. We put a drop of water suspension of the beads on the cover slip (#1.5 - the measured thickness of the coverslip 170 μm) a let it dry. This makes a flat (2D) sample.

The correction collar of the objective was adjusted to compensate for the spherical aberration. We set the correction collar such as we got an akin out-of-focus image of one individual bead while moving the plane of focus above and below the bead.

We reconstructed images for three different grating-periods of the excitation pattern (271 nm, 320 nm and 389 nm). The FWHM on 10 selected individual beads was estimated as described in section 5.1. The comparison of the experimental values with simulated data is shown in Fig. 5.7 and Table 5.4.

A detail of the reconstructed data for the pattern with a grating-period 320 nm is shown in Fig. 5.8. A wide-field image of the object is produced as a sum of acquired data for all different positions of the excitation pattern. For equal steps between the individual different positions of the pattern (within one orientation of the pattern), the sum yields a true wide-field image (see Eq.(2.20)).

$$\begin{aligned}\sum_{n=1}^{N} \tilde{Im}^{n}(\vec{k}) =& \sum_{n=1}^{N} \left[B_0\tilde{\rho}_0(\vec{k}) + \frac{1}{2}\left(B_{-1}e^{-i\left(2\frac{2\pi}{N}n+\phi_0\right)}\tilde{\rho}_{-1}(\vec{k}) + B_{+1}e^{i\left(2\frac{2\pi}{N}n+\phi_0\right)}\tilde{\rho}_{+1}(\vec{k})\right)\right] \\ =& NB_0\tilde{\rho}_0(\vec{k}) \end{aligned} \tag{5.3}$$

A direct comparison of the experimental data with the simulations shows that the experimental setup produces suboptimal results in a wide-field regime (see Fig. 5.7 and Table 5.4). The FWHM of the wide-field profile of the reconstructed experimental data is 1.3 to 1.6 times bigger than in the simulations. This might be due to the presence of aberrations in the imaging setup. The differences of the wide-field profiles in the images for different grating periods might be caused by a different setting of the correction collar. The data for the different grating periods were not taken in one single day and the setup was slightly re-aligned in the mean time.

The resolution improvement in the reconstructed images of fluorescent beads is obvious from Fig. 5.8 where we can clearly resolve the individual beads.

5.2.3 Biological Samples

The method was tested on biological samples as well. We used COS cells grown on the cover-slip stained with Alexa488 phalloidin to visualize the actin filaments and Arabidopsis cells labeled for microtubules and a gamma tubulin. The cells were embedded in ProLong® Gold anti-fade reagent (Invitrogen, USA). We acquired images with a rather long integration time (500 ms/image) to obtain good signal-to-noise ratio. The modified excitation pattern Eq.(2.40) with four different orientations (0°, 45°, 90° and 145°) was used. We took five images with different positions of the pattern (the lateral translation of the grid displayed on the SLM by an integer number of pixels) for every orientation. This yields 20 images required for the full reconstruction of the image.

Raw data for four different orientations of the excitation pattern are shown in Fig. 5.9(a-d). Corresponding Fourier transforms are shown in Fig. 5.9(e-h). Separated components for two orientations of the excitation pattern are shown in Fig. 5.10.

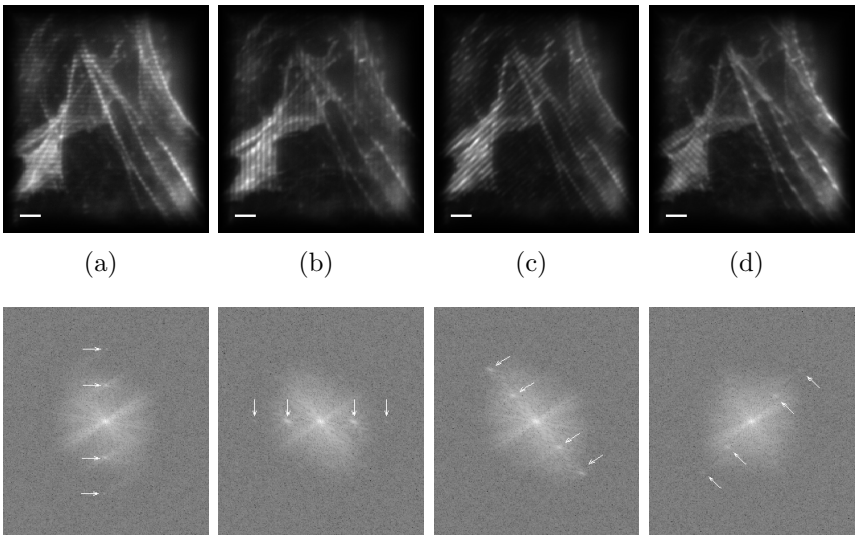

Figure 5.9: *Experimental data. Four orientations of the illumination pattern projected on the sample (a) 0˚, (b) 90˚ (c) 135˚ and (d) 225˚. Scale bar* $2\,\mu m$*. (e-h) Corresponding Fourier transforms in logarithmic scale. Five peaks are present because the modified excitation pattern Eq.*(2.40) *was used. White arrows point at* ± 2 *and* ± 1 *peaks in the Fourier transform.*

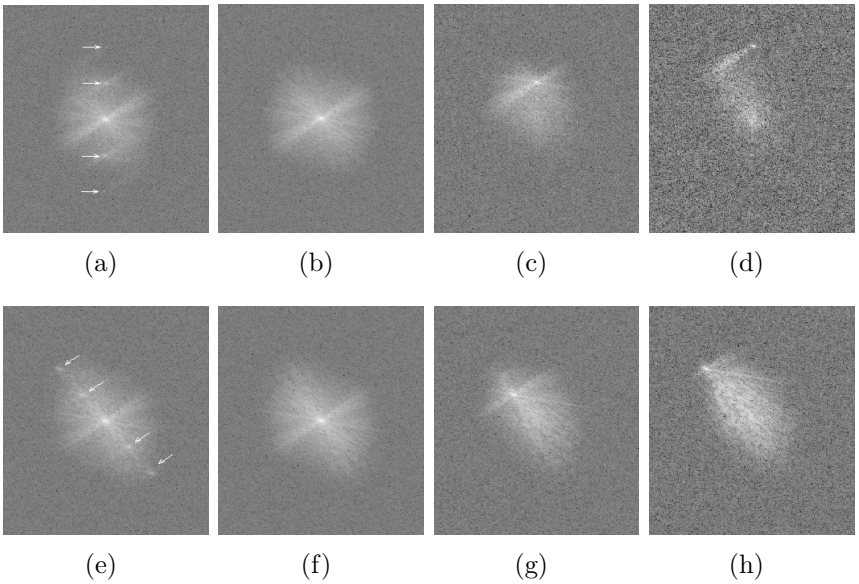

Figure 5.10: *Experimental data. Separation of individual components for two orientations of the illumination pattern (0˚ and 135˚). All images shown in logarithmic scale. (a, e) The Fourier transform of the data with arrows pointing to the* δ *peaks. (b, f) The separated components* $\tilde{\rho}_0$*, (c, g)* $\tilde{\rho}_{+1}$ *(d, h)* $\tilde{\rho}_{+2}$*.*

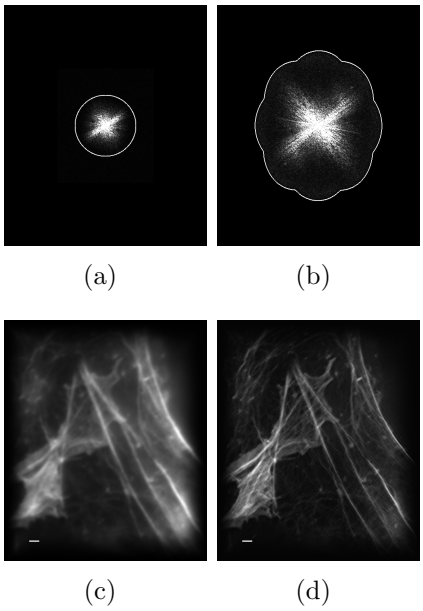

Figure 5.11: *Experimental data. (a) The Fourier transform of the wide-field image. Cut-off frequency border is marked with a white line. (c) The inverse Fourier transform of (a) represents an image from a classical wide-field microscope. (c) The reconstructed Fourier transform with an enlarged area of detectable Fourier frequencies. (d) The inverse Fourier transform of (c) represents the reconstructed image with an improved resolution. Scale bar* 1 μm.

The reconstructed image is shown in Fig. 5.11. Other reconstructed experimental data can be found in Appendix C.

We can observe that the out-of focus haze is suppressed in the reconstructed images of biological samples (see e.g.. Fig. C.2, C.3 or C.4 in Appendix C). This can be explained if we look at the full 3D situation of the OTF support enlargement in Fig. 5.12 and 5.13. The full 3D OTF support is enlarged along the lateral direction (k_x and k_y). At the same time the laterally translated 3D OTFs are filling the 'missing cone' area of the classical OTF. We get information about the spatial frequencies along the axial direction and so we get a sectioning in the reconstructed image.

The ability to fill the missing cone area depends on the parameters of the excitation pattern. If the harmonic pattern Eq.(2.13) is used, we have three components to separate. Three situations for different grating periods of the excitation patten are shown in Fig. 5.13(b-d). Note that in the case of the double resolution improvement (the frequency of the excitation pattern lies on the border of the OTF support: $2\,|\vec{\kappa}| = k_{cut}$) there is no filling of the missing cone area Fig. 5.13(d) and no sectioning is achieved in the reconstructed image. If we want to fill the missing cone, we have to sacrifice the lateral resolution and use the pattern with the lower frequency Fig. 5.13(b and c).

If we use the modified excitation pattern (see Eq.(2.40)), we get five components

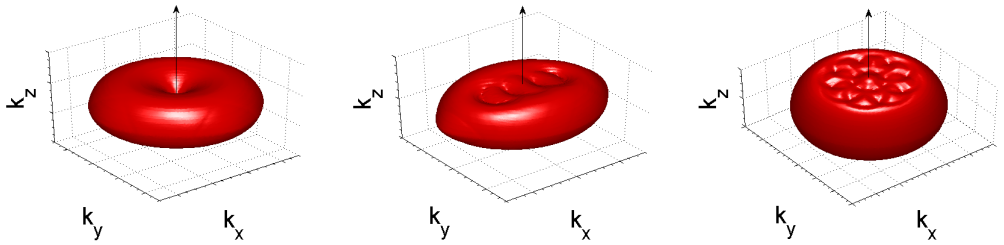

(a) (b) (c)

Figure 5.12: *A full 3D support of the OTF. (a) A classical wide-field OTF support. Note a "missing cone" along the axial direction (black arrow). (b) Full 3D combination of the three translated OTFs along the k_x direction (0˚). This represents a reconstruction with the excitation patter of $2|\vec{\kappa}| = 0.5k_{cut}$. (c) 3D combination of the shifted OTFs along four directions (0˚, 90˚, 135˚ and 225˚.). Note the filling of the 'missing cone' area.*

to separate (Eq.(2.41)) and it leads to the filling of the missing cone even in the case of the resolution doubling Fig. 5.13(e).

The full 3D reconstruction with the modified pattern Eq.(2.40) leads to seven components to separate (see Eq.(2.39)). In 3D Fourier space, they are in positions (see Eq.(2.39))

$$\begin{aligned} k_0 &= [0,\, 0,\, 0] \\ k_{1,\pm1} &= [\kappa_x,\, 0,\, \pm(\kappa - \kappa_z)] \\ k_{-1,\pm1} &= [-\kappa_x,\, 0,\, \pm(\kappa - \kappa_z)] \\ k_{\pm2} &= [\pm 2\kappa_x,\, 0,\, 0] \end{aligned}$$

and the reconstruction leads to the further resolution improvement along the z-axis (see Fig. 5.13(f)).

The ability of the method to achieve sectioning holds even if we make the reconstruction only in the focal plane. A two-dimensional in-focus wide-field image of the three-dimensional structure is a projection of the of the 3D structure $\rho(x, y, z)$ convolved with the 3D point spread function $\mathrm{PSF}(x, y, z)$ into the in-focus plane:

$$Im(x, y) = \int dz Im(x, y, z). \tag{5.4}$$

The two-dimensional Fourier transform yields:

$$\iint dxdy Im(x, y) e^{-i(k_x x + k_y y)} = \int dz \iint dxdy Im(x, y, z) e^{-i(k_x x + k_y y)}$$

which is the projection of the individual 2D Fourier transforms in every plane along the z-direction. This means that this 2D Fourier transform indeed contain encoded information about the frequencies in full 3D Fourier space. Even 2D manipulation with the separated components within the in-focus plane can still fill in the missing cone area in the reconstructed Fourier transform.

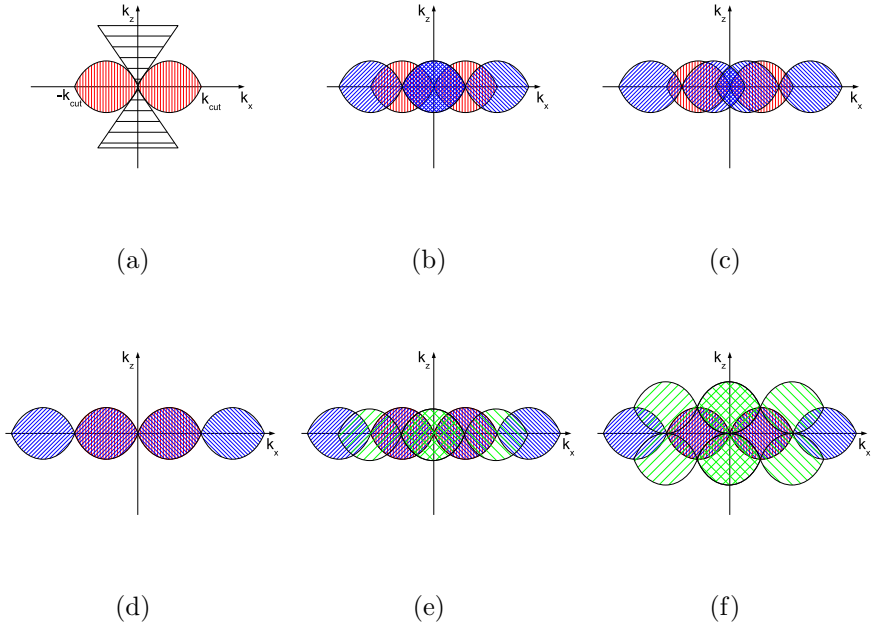

Figure 5.13: *An axial slice of the support of the 3D OTF. (a) A wide-field OTF with a 'missing cone' along the k_z axis (black stripes). k_{cut} is a cut-off frequency along the k_x axis. (b-d) Three separated components (± 1 component in blue) for the excitation pattern with a spatial frequency (b) $2\left|\vec{\kappa}\right| = 0.5k_{cut}$, (c) $2\left|\vec{\kappa}\right| = 0.75k_{cut}$, (d) $2\left|\vec{\kappa}\right| = k_{cut}$ (resolution doubling). (d) The use of the modified excitation pattern Eq.*(2.40) *yields five separated components. The missing cone area is filled even in the case of the resolution doubling. (d) Full three-dimensional reconstruction with the modified pattern yields seven separated components and leads to further resolution enhancement along the axial direction.*

5.2.4 Limits of the method

The linear relationship in Eq.(2.3) set a limit to the enlargement of the OTF support in the lateral plane. The experimental setup is in epi-fluorescence configuration and the objective is used both for the illumination of the sample and the acquisition of the fluorescent images. As the objective is incapable of detecting the spatial frequencies above the k_{cut} limit (Eq.(2.10)), it is not possible to generate an excitation pattern with a spatial frequency $\vec{\kappa}$ above this limit ($\left|\vec{\kappa}\right| \leq k_{cut}$). In other words, δ peaks in the Fourier transform of the excitation pattern cannot lie outside the support of the wide-field OTF (see Fig. 2.3(c)). The cut-off frequency border in the lateral plane can be extended twice in the limiting case where the δ peaks are located on the edge of the OTF support (the spatial frequency of the excitation pattern is the maximal possible that pass through the objective $2\left|\vec{\kappa}\right| = k_{cut}$). An illustration is shown in Fig. 5.14.

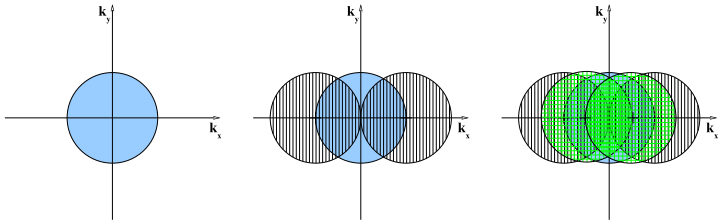

(a) (b) (c)

Figure 5.14: *Maximal extension of the cut-off frequency border. (a) The support of the classical wide-field OTF. (b) The maximal enlargement of the OTF support along the k_x direction for the excitation pattern Eq.*(2.13)*. The axial slice of this situation in 3D Fourier space is in Fig. 5.13(d). (b) The maximal enlargement of the OTF support along the k_x direction for the modified excitation pattern Eq.*(2.40)*. The axial slice in the 3D Fourier space is shown in Fig. 5.13(e). The position of the δ peaks is marked with black crosses.*

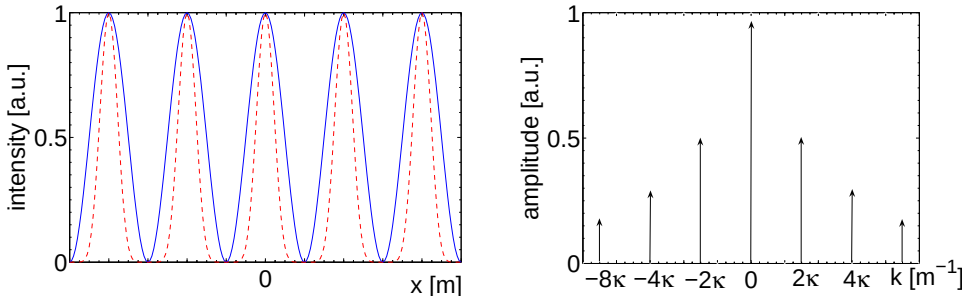

(a) (b)

Figure 5.15: *(a) A non-linear relationship between the illumination (a blue solid line) and the fluorescence emission (a red dashed line). An excitation pattern according to Eq.2.13 with spatial frequency 2κ. (b) The Fourier transform of the red dashed line contains higher harmonics. It is a set of δ peaks located in the integer multiples of the basic spatial frequency 2κ of the excitation pattern.*

Further resolution improvement is possible if the linear relation Eq.(2.3) is broken [26, 25]. An introduction of the nonlinear relationship between the excitation and the fluorescence emission results in the generation of higher harmonics components in the Fourier transform (see Fig. 5.15). δ peaks are located even in the region above the cut-off frequency k_{cut} of the wide-field OTF. The convolution with the Fourier transform of the sample $\tilde{\rho}$ results in a set of multiple copies of the $\tilde{\rho}$ in Fourier space (Fig. 5.16). All this components can be separated and shifted back as in the linear case (section 2.5.3). A theoretically unlimited resolution is possible with such

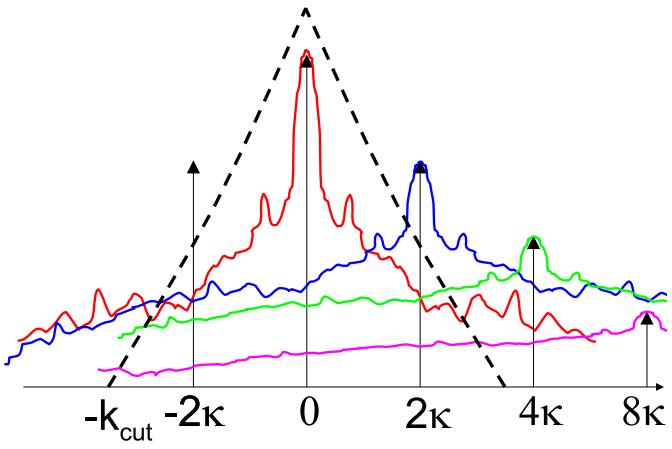

Figure 5.16: *A non-linear relationship between the illumination and the fluorescence emission leads to multiple copies of a classical component in the Fourier transform.*

a modification of the method. In the real experiment, the resolution is limited by a signal-to-noise ratio in the separated components.

5.2.5 Acquisition speed

A challenging task is to make a reconstruction of living biological samples. The basic requirement for the successful reconstruction is that the sample does not move during the data acquisition. The algorithm can correct for the lateral drift of the whole sample but an internal movement within the structure of the sample makes a faithful reconstruction impossible. For the reconstruction with an isotropic enlargement of the OTF support, we acquire data with four orientations of the excitation pattern (Fig. 2.8(d)). For every orientation, three (or five for modified pattern Eq.(2.40)) images with different translation of the pattern are required. This yields 12 (or 20) images needed for the reconstruction of one image. The integration time 100 ms/image, then gives 1.2 s (or 2 s) acquisition time per a data-set used for the reconstruction. In reality, this time is even longer as the rotation of the half-wave plate and the linear polarizer (see section 3) is required between the change of the pattern orientation. During the acquisition time (ca 5 s for the 100 ms exposure), the sample must stay perfectly still. This might set a limit for the reconstruction of quickly moving samples. The acquisition time can be shorten by reducing the number of the pattern orientation (e.g. three 0°, 120° and 240°) and by use of a powerful laser source.

Time required for the computation of the reconstructed image depends on the parameters of the computer. For our machine (AMD Athlon 64 Processor 3700+ at 2.21GHz with 1GB of RAM), the reconstruction of an image 512×512 pixels takes less than 10 minutes.

6 Conclusion

The theoretical predictions of the resolution improvement in the focal of the wide-field microscope using a spatially modulated excitation of the fluorescent sample was confirmed using simulated and experimental data. We developed the algorithm for the image reconstruction and we tested it using simulated at various noise levels including a noise free simulation. We also tested the ability of the algorithm to compensate for imperfections such as the drift of the sample, brightness fluctuation or imprecise translation of the excitation pattern. The size (FWHM) of the reconstructed simulated fluorescent beads was linearly dependent on the enlargement of the OTF support. The actual value of the FWHM depends on the shape of the apodization function and on the parameter of the Wiener filter used in the reconstruction.

The method was also applied to the reconstruction of real samples. The data were acquired on the experimental setup which we constructed in the laboratory of the Biological Nanoimaging research group in Randall Division in London. A comparison of the test-samples (100 nm fluorescent beads) with the simulated data reveals that the experimental setup produces suboptimal results in the wide-field regime. However, the behavior of the resolution improvement in the experimental data is consistent with the simulations. We achieved a nearly isotropic 1.78 times enlargement of the maximal detectable spatial frequency in the lateral plane. The resolution improvement is clearly visible in the comparison of the wide-field and the reconstructed image. The reconstructed images of biological samples also demonstrate the ability of the method to remove the out-of-focus haze in the image.

PEM is a relatively inexpensive method with a great potential in the biological science. The linear case discussed in this thesis, allows to achieved up to 2 times enlargement of the maximal detectable spatial frequency in the lateral plane. In a non-linear case further discussed in section 5.2.4, the resolution is limited only by a signal-to-noise ratio of the acquired data.

Appendix

A Mathematical Properties of the Fourier Transformation and Dirac Delta Distribution

A.1 Fourier Series

Fourier series decomposes a periodic function into a sum of complex exponentials. If $g(x)$ denotes a function of a real variable x, periodic with a period p ($g(x+p) = g(x)$) for all real numbers x and $\int_{-\frac{p}{2}}^{+\frac{p}{2}} dx \left|g(x)\right|^2 < \infty$ then [4]:

$$\lim_{N\to\infty} \sum_{n=-N}^{N} a_n e^{ik_n x} = g(x) \tag{A.1}$$

where $k_n = \frac{n2\pi}{p}$ and the coefficients a_n can be found by

$$a_n = \frac{1}{p}\int_a^{a+p} dx g(x) e^{-ik_n x} \tag{A.2}$$

We call Eq.(A.2) the Fourier transformation of the function $g(x)$ over a period p. The sum

$$S_N = \sum_{n=-N}^{N} a_n e^{ik_n x} \tag{A.3}$$

is called a partial sum which is an approximation of the function $g(x)$.

A.2 Fourier Transformation

Fourier transform is a mathematical operation which transforms one function defined in real space into another define in the space of spatial frequencies. The transformed function is called the spatial frequency ($\vec{k}$) domain representation of the original function. If $g(\vec{r})$ is a function (in general, complex valued) defined over $\mathbb{R}^n$, the Fourier transform (here represented by $\mathcal{F}\{g\}$) is by definition:

$$\mathcal{F}\{g\}(\vec{k}) = \int_{\mathbb{R}^n} d\vec{r}\; g(\vec{r}) e^{-i\vec{k}\cdot\vec{r}} \tag{A.4}$$

The inverse Fourier transform of the function $\tilde{g}(\vec{k})$ from frequency domain into space domain is:

$$\mathcal{F}^{-1}\{\tilde{g}\}(\vec{r}) = \int_{\mathbb{R}^n} d\vec{k}\; \tilde{g}(\vec{k}) e^{i\vec{k}\cdot\vec{r}} \tag{A.5}$$

While a variety of sets of sufficient conditions for the existence of Eq.(A.4) or Eq.(A.5) are possible, the most common set is the following [2]:

1. $g(\vec{r})$ must be absolutely integrable over the $\mathbb{R}^n$
2. $g(\vec{r})$ must have only a finite number of discontinuities and a finite number of maxima and minima in any finite area in $\mathbb{R}^n$
3. $g(\vec{r})$ must have no infinite discontinuities

In general, any one of these conditions can be weakened at the price of strengthening others.

If the function g is real, the Fourier transform is 'hermitian' symmetrical with respect to the origin:

$$\tilde{g}(\vec{k}) = \overline{\tilde{g}}(-\vec{k}). \tag{A.6}$$

Where dash above variables denotes the complex conjugation.

A.3 Shift Theorem

A translation in the space domain introduces a linear phase shift in the frequency domain:

$$\mathcal{F}\left\{g(\vec{r}-\vec{P})\right\} = e^{-i\vec{k}\cdot\vec{P}}\mathcal{F}\left\{g\right\}(\vec{k}) \tag{A.7}$$

Proof:

$$\begin{aligned}\mathcal{F}\left\{g(\vec{r}-\vec{P})\right\} &= \int_{\mathbb{R}^n} d\vec{r}\; g(\vec{r}-\vec{P})e^{-i\vec{k}\cdot\vec{r}} \\ &= \int_{\mathbb{R}^n} d\vec{r}' g(\vec{r}')e^{-i\vec{k}\cdot\left(\vec{r}'+\vec{P}\right)} \\ &= e^{-i\vec{k}\cdot\vec{P}}\mathcal{F}\left\{g\right\}(\vec{k}) \qquad \square\end{aligned}$$

A.4 Convolution Theorem

A convolution (denoted with symbol $\circledast$) of two functions $g(\vec{r})$ and $h(\vec{r})$ is defined:

$$\left[g(\vec{r}) \circledast h(\vec{r})\right](\vec{\xi}) = \int_{\mathbb{R}^n} d\vec{r}\; g(\vec{r})h(\vec{r}-\vec{\xi}). \tag{A.8}$$

Fourier transform of the convolution of two functions in one domain is entirely equivalent to the multiplication of their individual transforms in the other domain (*convolution theorem*):

$$\mathcal{F}\left\{g \circledast h\right\} = \mathcal{F}\left\{g\right\}\mathcal{F}\left\{h\right\}. \tag{A.9}$$

Proof:

$$\begin{aligned}\mathcal{F}\{g \circledast h\} &= \mathcal{F}\left\{\int_{\mathbb{R}^n} d\vec{r}\; g(\vec{r})h(\vec{r}-\vec{\xi})\right\} \\ &= \int_{\mathbb{R}^n} d\vec{r}\; g(\vec{r})\mathcal{F}\left\{h(\vec{r}-\vec{\xi})\right\} \\ &= \int_{\mathbb{R}^n} d\vec{r}\; g(\vec{r})e^{-i\vec{r}\cdot\vec{\xi}}\mathcal{F}\{h(\vec{r})\} = \mathcal{F}\{g(\vec{r})\}\,\mathcal{F}\{h(\vec{r})\} \qquad \square\end{aligned}$$

A.5 Shifting property of the Dirac δ distribution

Dirac δ distribution is a mathematical object defined by the following characteristics

$$\int_{\mathbb{R}^n} d\vec{r}\delta(\vec{r})f(\vec{r}) = f(0) \tag{A.10}$$

where $f(\vec{r})$ is a suitable test function. It can be viewed as a limit of the sequence of functions

$$\delta(\vec{r}) = \lim_{a\to 0} \frac{1}{a(\pi)^{n/2}} e^{-\frac{|\vec{r}|^2}{a^2}} \tag{A.11}$$

We define $\delta_{\vec{\rho}}(\vec{r}) \equiv \delta(\vec{r}-\vec{\rho})$ Dirac distribution shifted to the point $\vec{\rho}$. If we compute a convolution (Eq.(A.8)) of $\delta_{\vec{\rho}}(\vec{r})$ with $f(\vec{r})$ we get (using Eq.(A.10)):

$$\begin{aligned}\delta_{\vec{\rho}}(\vec{r}) \circledast f(\vec{r}) &= \int_{\mathbb{R}^n} d\vec{r}\;\; f(\vec{r})\delta_{\vec{\rho}}(\vec{r}-\vec{\xi}) \\ &= \int_{\mathbb{R}^n} d\vec{r}\;\; f(\vec{r})\delta(\vec{r}-[\vec{\xi}-\vec{\rho}]) \\ &= f(\vec{\xi}-\vec{\rho})\end{aligned} \tag{A.12}$$

which is the original function shifted by the amount $\vec{\rho}$. We call this *the shifting property* of the Dirac δ distribution.

B Auxiliary functions

B.1 "*findshift*"

This function determines a relative shift $\vec{P}$ of two input (real or complex) images I_1 and I_2. The shift is calculated from the position of the peak in the image of the absolute value of a weighted cross-correlation function X:

$$X_w(\vec{x}) = \frac{\iiint d\vec{\xi}\; w(\vec{\xi}) I_1(\vec{\xi}) w(\vec{\xi}+\vec{x}) I_2^*(\vec{x}+\vec{\xi})}{\iiint d\vec{\xi}\; w(\vec{\xi}) w(\vec{\xi}+\vec{x})} \tag{B.1}$$

where $w(\vec{\xi})$ is the weight for every pixel. A rough guess of the shift is inserted as an input parameter in case that there are more than one principal peaks. This can happen if the separation of the components is imperfect or a noise level is too high and the similarity between two images is suppressed.

A cross-correlation function Eq.(B.1) is used for real images. For complex valued images, such as separated components in Fourier space $\tilde{\rho}_m(\vec{k}) = \left|\tilde{\rho}_m(\vec{k})\right| e^{i\theta_m(\vec{k})}$, where$|\tilde{\rho}_m|$ is an absolute value of the $\tilde{\rho}_m(\vec{k})$ and $e^{i\theta_k(\vec{k})}$ is a phase map of the components, a weighted cross-correlation function can be optionally computed from phase information only.

$$X_w^{\text{phase}}(\vec{x}) = \frac{\iiint d\vec{\xi}\; w(\vec{\xi}) e^{i\theta_1(\vec{\xi})} w(\vec{\xi}+\vec{x}) e^{-i\theta_2(\vec{\xi}+\vec{x})}}{\iiint d\vec{\xi}\; w(\vec{\xi}) w(\vec{\xi}+\vec{x})}. \tag{B.2}$$

For an optimal signal-to-noise ratio, the (real) weights $w(\vec{\xi}) = \left|OTF(\vec{\xi})\right|$ can be used.

The position of the peak $\vec{P}$ (with sub-pixel precision) in the absolute value of the cross-correlation function X_w is determined in a certain area around the estimated location. It is found by a function "*findRelMax*" (Appendix B.2). The value $\vec{P}$ is used for the shift of one of the image $I_1(\vec{\xi}-\vec{P})$ in Eq.(B.1) or Eq.(B.2) and the cross-correlation is computed again. The value of the central pixel $\vec{x} = 0$ of the cross-correlation

$$X_w(0) = \frac{\iiint d\vec{\xi}\; w(\vec{\xi}) I_1(\vec{\xi}-\vec{P}) w(\vec{\xi}) I_2^*(\vec{\xi})}{\iiint d\vec{\xi}\; w(\vec{\xi}) w(\vec{\xi})}$$

is maximized by an iterative procedure varying the shift $\vec{P}$ with sub-pixel precision.

B.2 "*findRelMax*"

Estimates the position $\vec{P}$ of the peak in the input (real) image $I(\vec{r})$ with sub-pixel precision. The peak is searched in a certain area around the estimated position (a rough guess).

The sub-pixel precision is achieved by computing a center of masses of a 'Hat' of the peak. The 'Hat' is obtained by removing the values that are below a threshold value (a fraction of the maximal value of the detected peak) from $I(\vec{r})$ and by subtracting the threshold value.

$$\vec{P} = \frac{\int d\vec{r}\ \vec{r} Hat(\vec{r})}{\int d\vec{r}\ Hat(\vec{r})}.$$

C Image Gallery

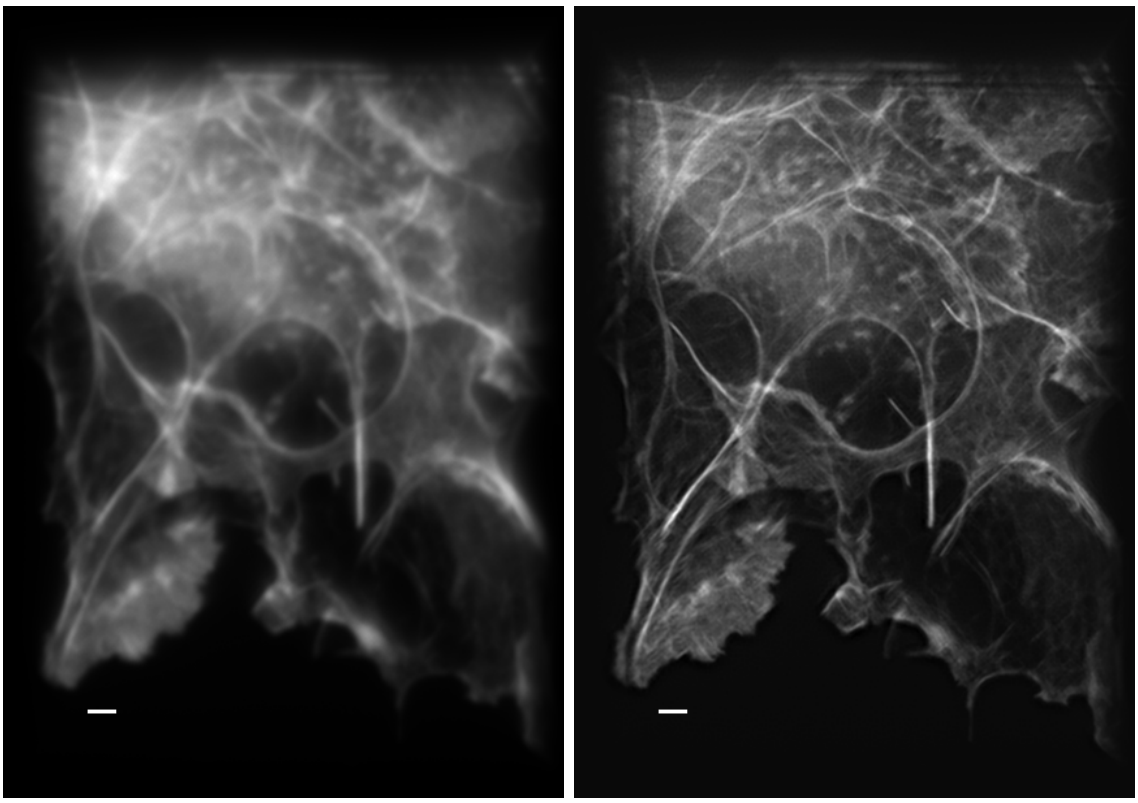

(a) (b)

Figure C.1: *COS cells, actin filaments. (a) Wide-field image. (b) Reconstructed image (modified excitation pattern with a grating period of 271 nm). Scale bar* 1 μm. *Samples kindly provided by Elizabeth Ehler.*

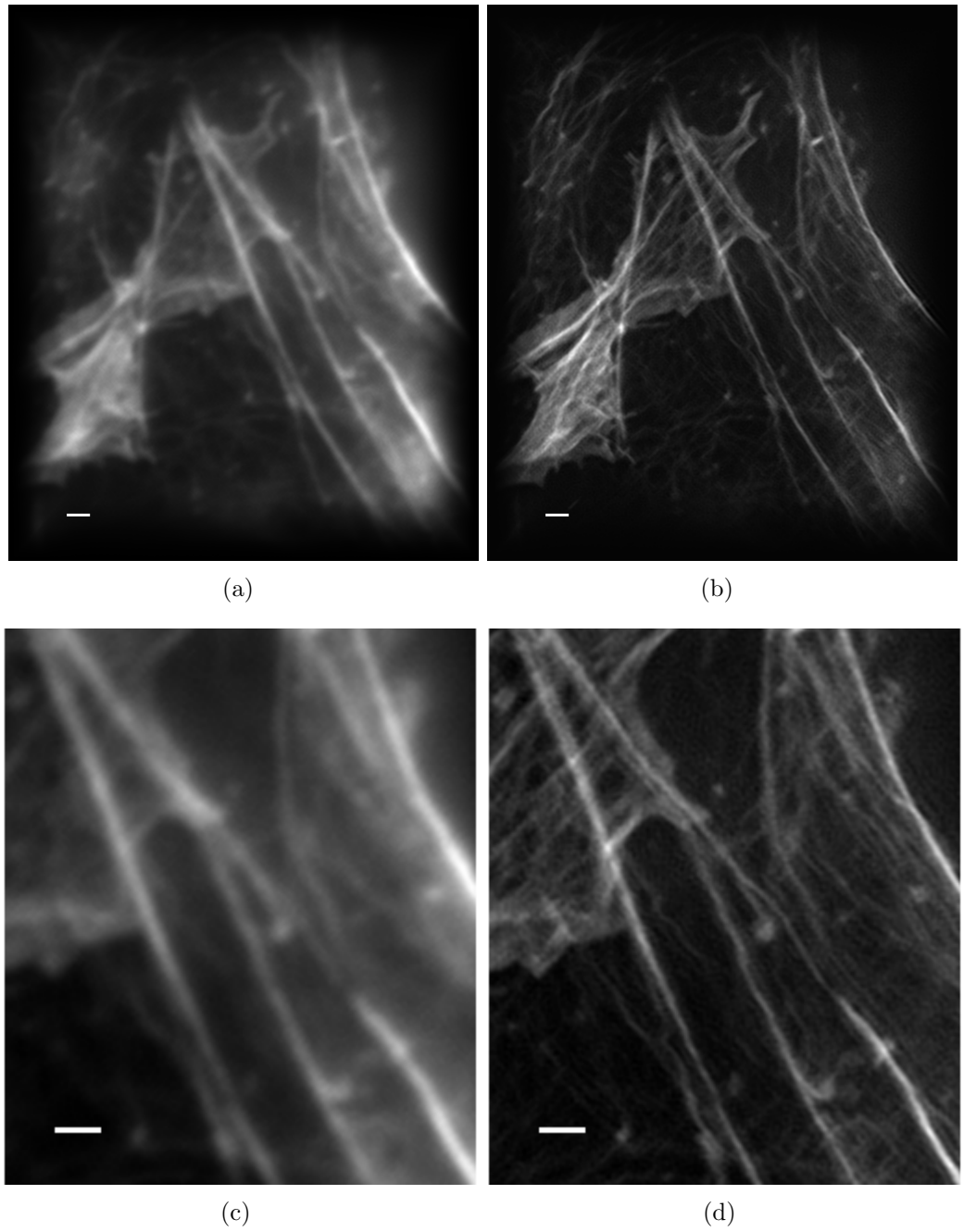

(a) (b)

(c) (d)

Figure C.2: *COS cells, actin filaments. (a) Wide-field image. (b) Reconstructed image (modified excitation pattern with a grating period of 271 nm). (c, d) A detail of the images above. Scale bar* 1 μm. *Samples kindly provided by Elizabeth Ehler.*

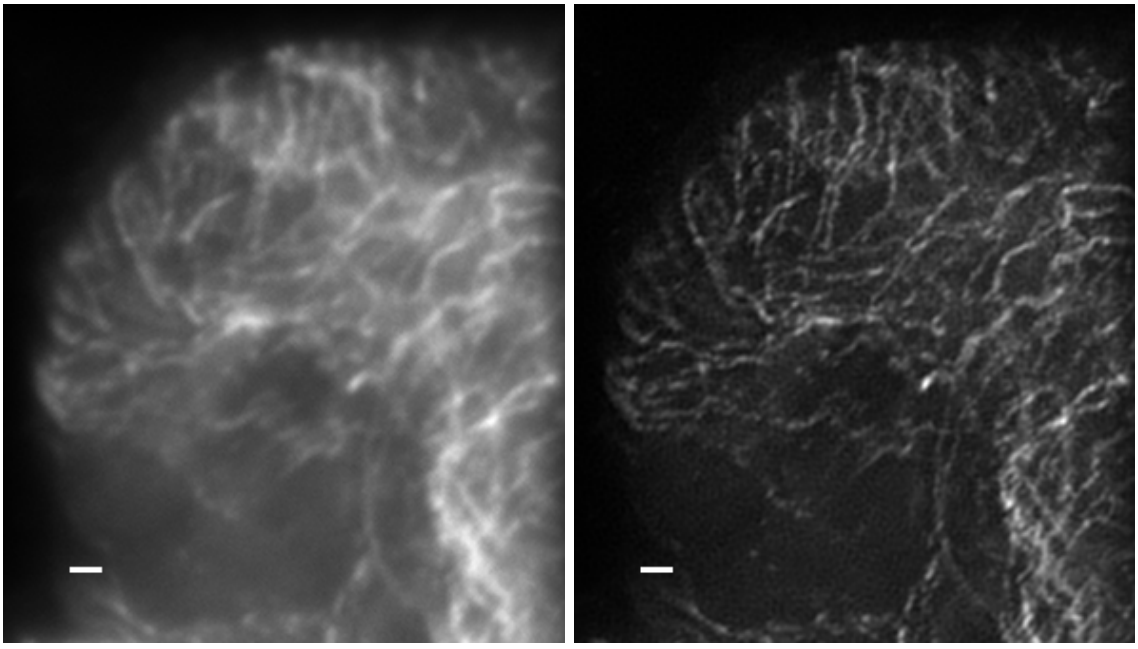

(a) (b)

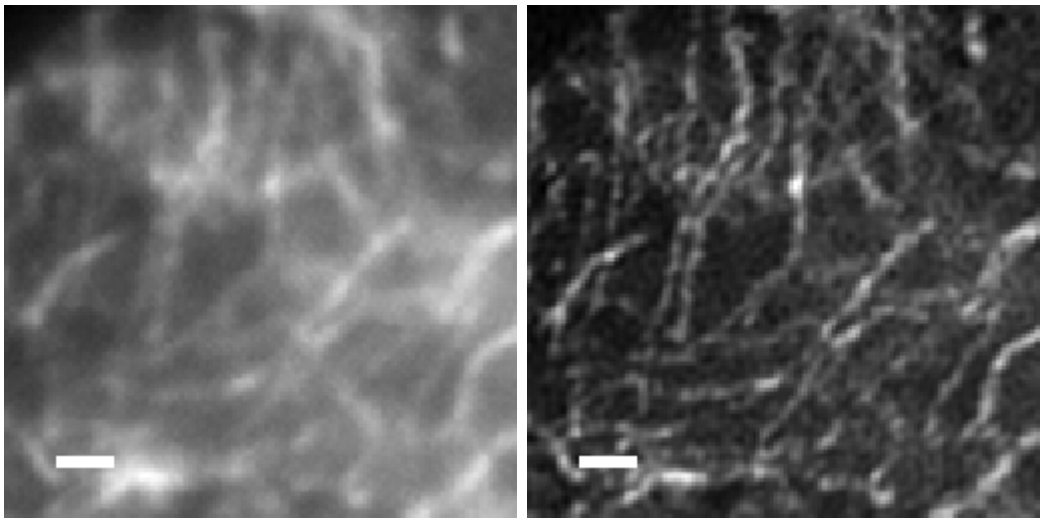

(c) (d)

Figure C.3: *Arabidopsis cells labeled for microtubules and a gamma tubulin. (a) Wide-field image. (b) Reconstructed image (modified excitation pattern with a grating period of 320 nm). (c, d) A detail of the images above. Scale bar* 1 μm. *Samples kindly provided by Jiří Hašek.*

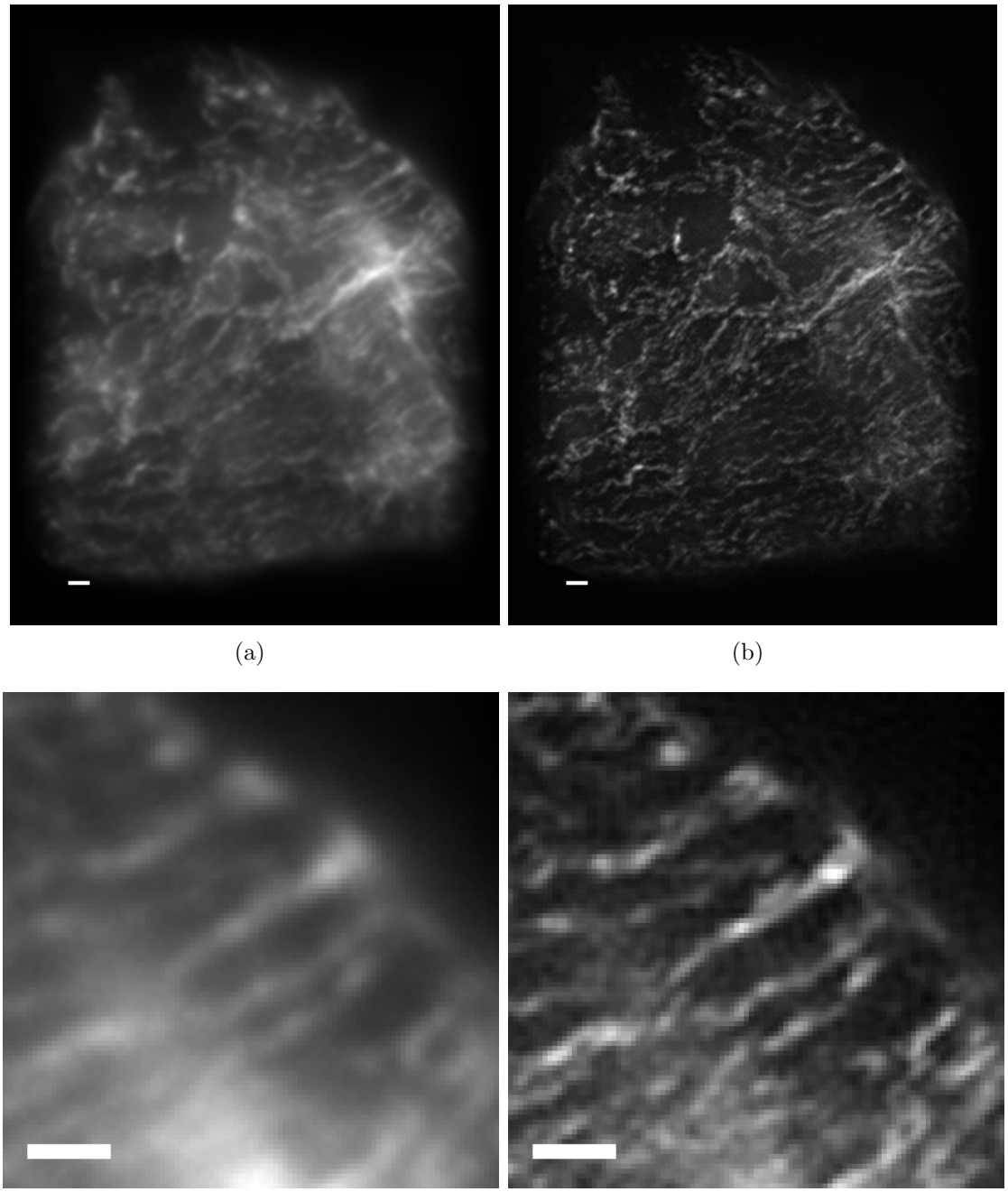

(a) (b)

(c) (d)

Figure C.4: *Arabidopsis cells labeled for microtubules and gamma tubulin. (a) Wide-field image. (b) Reconstructed image (modified excitation pattern with a grating period of 320 nm). (c, d) A detail of the images above. Scale bar* 1 μm. *Samples kindly provided by Jiří Hašek.*

References

[1] E. Abbe, "Beiträge zür Theorie des Mikroskops und der mikroskopichen Wahrnehmung," (1873) in Arkiv Mikroskopiche Anat. 9, pp. 413 - 468.

[2] J.W. Goodman, "Introduction to Fourier Optics" (1968) McGraw-Hill Companies.

[3] M. Born, E. Wolf, "Principles of Optics," (1999) 7th edition, Cambridge University Press.

[4] J. W. Gibbs, "Fourier Series" (1899) Nature 59, 200.

[5] V. Westphal, S. W. Hell, "Nanoscale Resolution in the Focal Plane of an Optical Microscope," (2005) Phys. Rev. Lett. 94, 143903.

[6] S. Hell, E. H. K. Stelzer, "Properties of a 4Pi confocal fluorescence microscope," (1992) J. Opt. Soc. Am. A 9, 2159 - 2166.

[7] J. B. Pawley, "Handbook of Biological Confocal Microscopy," (1995), Plenum Press, New York.

[8] M. Petran, M. Hadravsky, M.D. Egger, R. Galambos, "Tandem-Scanning Reflected-Light Microscope," (1968) J. Opt. Soc. Am. 58, p. 661.

[9] M.D. Egger, "The development of confocal microscopy," (1989) Trends Neurosci. 12:11.

[10] T. Wilson, "The role of the pinhole in confocal imaging system," (1995) Handbook of Biological Confocal Microscopy (ed. by J.B. Pawley), Plenum Press, New York, pp. 167-182.

[11] H. Gugel et al. "Cooperative 4Pi excitation and detection yields 7-fold sharper optical sections in live cell microscopy," (2004) Biophys J. 87, pp. 4146-5152.

[12] V. Westphal, L. Kastrup & S.W. Hell, "Lateral resolution of 28 nm ($\lambda/25$) in far-field fluorescence microscopy," (2003) Appl. Physi. B 77, pp. 189-193.

[13] M.G.L. Gustafsson, "I^5M: 3D widefield light microscopy with better than 100 nm axial resolution," (1999) Journal of Microscopy 195, pp. 10-16.

[14] M.G.L. Gustafsson, Lin Shao, Peter M. Carlton, C. J. Rachel Wang, Inna N. Golubovskaya, W. Zacheus Cande, David A. Agard, and John W. Sedat, "Three-dimensional Resolution Doubling in Widefield Fluorescence Microscopy by Structured Illumination," (2008) Biophys. J.; Published ahead of print on March 7, 2008 as doi:10.1529/biophysj.107.120345.

[15] Lin Shao, Berith Isaac, Satoru Uzawa, David A. Agard, John W. Sedat, and M.G.L. Gustafsson, "I5S: Widefield Light Microscopy with 100-nm-scale Resolution in Three Dimensions," (2008) Biophys. J.; Published ahead of print on March 7, 2008 as doi:10.1529/biophysj.107.120352.

[16] J.T. Frohn, H.F. Knapp, A. Stemmer, "Three-dimensional resolution enhancement in fluorescence microscopy by harmonic excitation," (2001) Opt. Lett. 26, pp. 828-830.

[17] R. Heintzmann, C.G. Cremer, "Laterally modulated excitation microscopy: improvement of resolution by using a diffraction grating," (1999) Proc. SPIE 3568, pp. 185-196.

[18] R. Heintzmann, "Band Limit and Appropriate Sampling in Microscopy," in Cell Biology, Laboratory Handbook (Volume 3), 3rd ed., J. E. Celis, (Elsevier, London, 2006), pp. 29-36.

[19] R. Y. Tsien and A. Waggoner, "Flourophores for confocal microscopy," in Handbook of Biological Confocal Microscopy, 2nd ed., J. B. Pawley, ed. (Plenum Press, New York, 1995), pp. 267-268.

[20] D. R. Sandison, R. M. Williams, K. S. Wells, J. Strickler and W. W. Webb, "Quantitative fluorescence confocal laser scanning (CLSM) microscopy," in Handbook of Biological Confocal Microscopy, 2nd ed., J. B. Pawley, ed. (Plenum Press, NewYork, 1995), pp. 47-50.

[21] M.A.A. Neil, R. Juskaitis and T. Wilson, "Method of obtaining optical sectioning by using structured light in a conventional microscope," (1997) Optics Letters 22, pp. 1905-1907.

[22] R. Heintzmann, "Structured Illumination Methods," in Handbook of Biological Confocal Microscopy, 3rd ed., J. B. Pawley, ed. (Plenum Press, NewYork, 2006), pp. 47-50.

[23] M.G.L. Gustafsson, D. A. Agard and J. W. Sedat, "Doubling the lateral resolution of wide-field fluorescence microscopy using structured illumination," (2000) SPIE 3919, pp. 141-150.

[24] R. Heintzmann and T.M. Jovin, "Saturated patterned excitation microscopy a concept for optical resolution improvement," (2002) J. Opt. Soc. Am. A 19, pp. 1599-1607.

[25] M.G.L. Gustafsson, "Nonlinear structured-illumination microscopy: Wide-field fluorescence imaging with theoretically unlimited resolution," (2005) Proc. Natl. Acad. Sci. 102, pp. 13081-13086.

[26] R. Heintzmann, "Saturated patterned excitation microscopy with two-dimensional excitation patterns," (2003) Micron 34, pp. 283-291.

[27] M.G.L. Gustafsson, "Surpassing the lateral resolution limit by factor of two using structured illumination microscopy," (2000) Journal of Microscopy 198, pp. 82-87.

[28] K. Wicker, "Resolution Improvement for Fluorescence Microscopy," (2007) PhD progress report.

[29] L. H. Schaefer, D. Schuster and J. Schafer, "Structured illumination microscopy: artefacts analysis and reduction utilizing a parameter optimization approach," (2004) Journal of Microscopy 216, pp. 165-174.

[30] A. Egner, S. W. Hell, "Equivalence of the Huygens-Fresnel and Debaye approach for the calculation of high aperture point-spread function in the presence of refractive index mismatch," (1999) Journal of Microscopy 193, pp. 224-249

[31] B. Richards, E. Wolf, "Electromagnetic Diffraction in Optical Systems. I. An Integral Representation of the Image Field," (1959) Proc. of the Royal Society of London. Series A, Mathematical and Physical Sciences, Vol. 253, No. 1274, pp. 349-357.

[32] private communication with R. Heintzmann

[33] http://www.ph.tn.tudelft.nl/DIPlib/

[34] R. Heintzmann, "Estimating missing information by maximum likelihood deconvolution," (2007) Micron 38, pp. 136–144.